Research Square

Preprints are preliminary reports that have not undergone peer review.
They should not be considered conclusive, used to inform clinical practice,
or referenced by the media as validated information.

Glucose Deprivation-Mediated Disulfide Stress Induces Cell Death in FHdeficient Renal Cell Carcinoma

Guowang Xu

xugw@dicp.ac.cn

Dalian Institute of Chemical Physics, Chinese Academy of Sciences https://orcid.org/0000-0003-4298-3554

Peng Dou

Dalian Institute of Chemical Physics, Chinese Academy of Sciences

Xin Lu

Dalian Institute of Chemical Physics, Chinese Academy of Sciences

Pengyu Geng

Dalian Institute of Chemical Physics, Chinese Academy of Sciences

Yasemin Cole

National Institutes of Health

Mlao Bao

Dalian Institute of Chemical Physics, Chinese Academy of Sciences

Xin Ge

Nanjing Medical University

Siming Pu

Dalian Institute of Chemical Physics, Chinese Academy of Sciences

Lina Zhou

Dalian Institute of Chemical Physics, Chinese Academy of Sciences

Xinyu Liu

Dalian Institute of Chemical Physics, Chinese Academy of Sciences https://orcid.org/0000-0002-0564-7167

Hang Li

Dalian Institute of Chemical Physics, Chinese Academy of Sciences

Jinhui Zhao

Dalian Institute of Chemical Physics, Chinese Academy of Sciences

Fating Chen

Dalian Institute of Chemical Physics, Chinese Academy of Sciences

Zhikun Lin

Dalian Institute of Chemical Physics, Chinese Academy of Sciences
Ting Wang
Dalian Institute of Chemical Physics, Chinese Academy of Sciences
Qi Li
Dalian Institute of Chemical Physics, Chinese Academy of Sciences
Jianwen Hu
Shanghai Bioprofile Technology Company Ltd.
Jie Dai
Shanghai Bioprofile Technology Company Ltd.
Xu Qian
Nanjing Medical University https://orcid.org/0000-0003-1533-8568
Zhengping Zhuang
National Institutes of Health https://orcid.org/0000-0002-0009-7370

Article

Keywords:

Posted Date: February 17th, 2025

DOI: https://doi.org/10.21203/rs.3.rs-5880350/v1

License: This work is licensed under a Creative Commons Attribution 4.0 International License.
Read Full License

Additional Declarations: There is **NO** Competing Interest.

Version of Record: A version of this preprint was published at Nature Communications on October 5th, 2026. See the published version at https://doi.org/10.1038/s41467-026-78274-6.

Abstract

$FH^{deficient}$ renal cell carcinoma (RCC) is a highly metastatic and challenging malignancy. Here, we show that the aberrant accumulation of intracellular disulfides in $FH^{deficient}$ cells leads to actin cytoskeleton contraction and induces a caspase-independent form of cell death. However, inhibition of Rho-associated coiled-coil containing protein kinase (ROCK) (which regulates actin cytoskeleton contraction) suppresses $FH^{deficient}$ cell death. Under glucose starvation, $FH^{deficient}$ cells attempt to mitigate NADPH consumption by downregulating the reductive tricarboxylic acid (TCA) cycle. However, defects in the oxidative TCA cycle prevent them from maintaining NADPH balance. Moreover, targeting mitochondrial complex I in $FH^{deficient}$ cells enhances the reductive TCA cycle while weakening the oxidative TCA cycle, thereby accelerating intracellular disulfide accumulation, tumor growth is significantly inhibited under low glucose conditions. Our study uncovers a caspase-independent cell death mechanism driven by disulfide stress and provides a potential therapeutic strategy targeting the metabolic vulnerability of $FH^{deficient}$ RCC.

Introduction

Tumors with abnormal expression or loss of metabolic enzymes often become highly dependent on specific metabolites for survival[1–3]. By restricting the uptake of these metabolites, it is possible to selectively target and kill tumor cells while sparing normal cells. A notable example is tumors with high expression of SLC7A11. These tumor cells are highly dependent on intracellular GSH, and interfering with its synthesis can promote ferroptosis[4–6]. However, these cells also exhibit glucose dependency. Under glucose deprivation, reduced NADPH production through the pentose phosphate pathway (PPP) leads to excessive consumption of cystine, which in turn causes an overload of disulfide accumulation in SLC7A11-high-expression tumors, ultimately triggering tumor cell death[7].

Fumarate hydratase (FH) catalyzes the conversion of fumarate to malate in the TCA cycle. As a tumor suppressor, FH is often mutated and inactivated in multiple tumor types, such as $FH^{deficient}$ renal cell carcinoma (RCC), resulting in the abnormal accumulation of the oncometabolite fumarate that promotes tumorigenesis through phosphatase and tensin homolog deleted on chromosome ten (PTEN) inactivation, hypoxia inducible factor (HIF) activation and epigenetic modulation of DNA and histone demethylases[8–12]. Moreover, tumor-derived fumarate can inhibit the activity of CD8 + T cells, thereby suppressing tumor immunity[13]. These factors contribute to the high malignancy and treatment resistance of $FH^{deficient}$ RCC. In this study, we reveal a new mode of cell death and a unique metabolic vulnerability in $FH^{deficient}$ RCC, and propose therapeutic strategies aimed at targeting this vulnerability to treat $FH^{deficient}$ RCC.

Results

Glucose starvation induces cell death in $FH^{deficient}$ cells by disulfides stress

To determine whether $FH^{deficient}$ RCC undergoes cell death under glucose starvation, we overexpressed FH in the naturally $FH^{deficient}$ UOK262 cells and knocked down FH (KD-FH) in 786-O cells. Under glucose starvation, we found that cell death in $FH^{deficient}$ UOK262 cells and FH knock-down 786-O cells significantly increases in a time-dependent manner under glucose starvation (Fig. 1A -1D). Subsequently, HeLa cells were treated with varying concentrations of fumarate hydratase inhibitor (FH-IN1) to inhibit FH activity (FH^{Inact}). As FH activity was progressively inhibited, cell death gradually increased in HeLa cells under glucose starvation (Fig. 1E and 1F). To characterize the nature of this cell death, we treated the cells with inhibitors specific to programmed necrosis (Nec-1 and Nec-2), apoptosis (Z-VAD-FMK, Z-VAD), ferroptosis (ferrostatin-1, Ferr-1), and autophagy (chloroquine, CQ). The results showed that these inhibitors did not rescue glucose-starved FH^{Inact} HeLa cells from death (Fig. 1G). In contrast, disulfide bond scavengers such as Dithiothreitol (DTT) and Tris (2-carboxyethyl) phosphine (TCEP) effectively rescued glucose-starved $FH^{deficient}$ UOK262 or FH^{Inact} HeLa cells from death (Figs. 1H and 1I). Given that disulfide scavengers could inhibit glucose starvation-induced cell death in $FH^{deficient}$ cell, this type of cell death was caused by the accumulation of abnormal disulfides.

The most significant effect of glucose starvation is the lack of NADPH provided by the pentose phosphate pathway (PPP), thereby diminishing the ability to reduce disulfides. To address this, under glucose-free conditions, we used 2-Deoxy-D-glucose (2DG), a glucose analog, to inhibit glycolysis and promote NADPH production through the PPP only[7]. Further analysis using capillary electrophoresis-mass spectrometry (CE-MS) demonstrated that 2DG reduced glycolysis metabolite fructose-6-phosphate (F6P), while promoting the conversion of 2DG to 2-Deoxyglucose-6-phosphate (2DG-6P) and increasing intracellular NADPH levels and effectively preventing $FH^{deficient}$ UOK262 cell death under glucose starvation (Figs. 1J, 1K and 1L). Therefore, these results suggested that $FH^{deficient}$ cells undergo disulfide stress-induced cell death under glucose starvation due to NADPH depletion.

Based on our observations, we found that the cell death of $FH^{deficient}$ cells shares similar characteristics with $SLC7A11^{high}$ cells death under glucose starvation, such as disulfide accumulation and inhibition of cell death by TCEP and DTT[7]. Next, we employed a redox proteomic approach to quantitatively analyze disulfide bonds between protein molecules (Fig. 1M). Under glucose starvation, we identified 679 upregulated cysteine-containing peptide segments from $FH^{deficient}$ UOK262 (Table S1). Gene Ontology (GO) analysis revealed a significant enrichment of biological processes and pathways related to the cadherin or cell adhesion molecular binding and actin filament or actin binding in the proteins exhibiting glucose starvation-induced disulfide bond accumulation in $FH^{deficient}$ UOK262 cells (Fig. 1N). Meanwhile, actin cytoskeleton-associated proteins, such as filamin-A/B (FLNA/B) and ACTN4, actin-cytoskeleton regulatory proteins, such as RAC1 and GSN, contain numerous cysteine sites and form disulfide bonds under glucose starvation (Figure S1O). We performed protein interaction network analysis on proteins

with the highest number of disulfide bonds (number ≥ 4). GO analysis revealed that 11 out of 24 proteins are involved in cell junction (blue circle) and cytoskeleton (red circle) (Fig. 1). The accumulation of disulfides in cell structural proteins, such as cell junction and cytoskeleton proteins, leading to severe disruption of cellular structure, might be the primary cause of cell death in $FH^{deficient}$ cells under glucose starvation. Next, we used electron microscopy to examine cell morphology. The result showed that plasma membrane separation (black arrows) in FH^{Inact} HeLa cells under glucose starvation (Figure S1A). 3D immunofluorescence cell imaging was employed to analyze the distribution of F-actin during cell death. The results showed that F-actin aggregates in FH^{Inact} HeLa cells under glucose starvation (Figure S1B). Next, SLC3A2 (indicating the cellular membrane position) and F-actin were labeled in $FH^{deficient}$ UOK262 cells, as illustrated in Fig. 1Q. The results showed that the plasma membrane and actin cytoskeleton of $FH^{deficient}$ UOK262 cells were separated under glucose starvation (white dashed lines indicate the boundary of the actin cytoskeleton). To confirm the aggregation of these actin cytoskeleton-associated proteins linked by disulfide bonds in $FH^{deficient}$ cells under glucose starvation, we performed non-reducing immunoblot analysis on actin cytoskeleton-associated proteins including FLNA, Drebrin, MYH9, and TLN1 in $FH^{deficient}$ UOK262 cells. The results showed that under glucose starvation, these actin cytoskeleton-associated proteins in $FH^{deficient}$ cells appeared in high-molecular-weight regions in their non-reduced states, suggesting that these proteins form oligomers through disulfide bonds (Fig. 1R). Excessive accumulation of ROS can promote the oxidation of cysteine residues in cellular proteins, leading to the formation of disulfide bonds[14]. Next, we treated FH^{Inact} HeLa cells with ROS scavengers Tempol and Trolox. The results showed that these ROS scavengers did not prevent glucose-starved FH^{Inact} HeLa from cell death (Figure S1C). Moreover, actin cytoskeleton- associated protein polymerization was not affected by ROS scavengers (Figure S1D and S1E). Therefore, the results suggested that the cell death caused by the accumulation of disulfides in $FH^{deficient}$ cells under glucose starvation was primarily due to a decrease in reducing agents (NADPH, GSH), rather than an increase in oxidant (ROS).

Next, we added propidium iodide (PI) to the culture medium to analyze cell membrane permeability and stained F-actin and the nucleus. Then, live-cell imaging was used to analyze the changes in the actin cytoskeleton and cell membrane permeability over time. The results showed that with prolonged glucose starvation, the cell cytoskeleton (green, F-actin) underwent continuous contraction, leading to the disruption of cell-cell junctions (white arrows in the magnified image). Ultimately, this resulted in altered membrane permeability (red, propidium iodide) and triggered cell death (Figure S1F and Video 1). This result indicated that actin cytoskeletal contraction occurs first, followed by cell membrane rupture. Rho-associated coiled-coil containing protein kinase (ROCK) regulates the cytoskeleton in various forms of cell death, playing a crucial role in facilitating cell death[15]. ROCK activates myosin light chain (MLC) phosphorylation, promoting the contraction of the actin cytoskeleton, which leads to plasma membrane rupture[16] (Figure S1G). To investigate this, we treated cells with various small-molecule inhibitors targeting ROCK and myosin and assessed cell death using a CCK-8 assay. The results showed that inhibition of ROCK and myosin activity reduced cell death induced by glucose starvation in $FH^{deficient}$

cells to varying extents (Figure S1H). Further treatment with a ROCK inhibitor suppressed the morphological contraction of $FH^{deficient}$ cells under glucose starvation (Figure S1I). Additionally, Non-reducing immunoblot analysis demonstrated that ROCK inhibition decreased the formation of myosin protein aggregates via disulfide bonding (Figure S1J). These findings indicated that inhibiting ROCK activity could suppress $FH^{deficient}$ cell death.

Inactivation of the caspases during disulfide stress in FH cells under glucose starvation

FH deficiency can directly lead to mitochondrial dysfunction. while abnormal mitochondrial function is often linked to the activation of various cell death pathways[17–20]. Next, mitochondria were isolated from FH^{Inact} cells (Figure S2A). Quantitative proteomics showed significant downregulation in actin-cytoskeleton associated proteins like FLNA, FLNB, and MYH9 in the mitochrodira of FH^{Inact} MCF-7 cells (Figure S2B and S2C). Immunofluorescence revealed that glucose starvation caused mitochondria (red) to compress around the nucleus due to actin cytoskeleton contraction (green) (Figure S2D). Drebrin polymerization under non-reducing conditions serves as a marker of cellular disulfide stress. Immunoblotting further revealed that under disulfide stress, proapoptotic protein BAX did not translocate to mitochondria (Figure S2E). Although we observed a partial reduction in mitochondrial membrane potential in FH^{Inact} HeLa cells under glucose starvation (Figure S2F), compared to Staurosporine (STS)-induced apoptosis, $FH^{deficient}$ and FH^{Inact} cells did not activate Caspase-3 under glucose starvation (Figure S2G). Why glucose starvation-induced cell death in $FH^{deficient}$ cells did not activate the caspase pathway was unexpected. We hypothesized that disulfide stress did not activate caspases because caspases undergo polymerization, similar to actin cytoskeleton associated proteins, resulting in a loss of activity. To test this hypothesis, we induced cell death in FH^{Inact} HeLa cells and assessed caspases aggregation using non-reducing immunoblotting. The results supported our hypothesis, showing that various caspases aggregated in response to disulfide stress (Fig. 2A and S2H), while Caspase-3 was observed in a dimerized form (Fig. 2B).

Next, to identify which cysteine(s) were involved in the dimerization of Caspase-3, molecular docking was performed and results indicated that Caspase-3 forms a disulfide bond between the cysteine residues at positions 184 (C184) and 264 (C264) of another Caspase-3, leading to dimer formation (Fig. 2C). Next, we constructed serine mutants of Caspase-3 at C184 and C264 (C184S, C264S, and C184, 264S). Following the induction of disulfide stress, the mutants C184S and C264S significantly suppressed the formation of Caspase-3 dimers (red arrow) and led to the formation of a polymer (Fig. 2D, red frame). Meanwhile, under glucose starvation, the Caspase-3 dimers could not be reduced by ROS scavengers (Troxol) but could be reduced by 2DG (Fig. 2E). To explore the potential systemic inactivation of caspases due to their aggregation in cells undergoing disulfide stress in $FH^{deficient}$ cell, we activated the caspase pathway using TNF-α and STS, and the results indicated that inhibiting FH activity in HeLa cells effectively prevented STS and TNF-α from activating caspases under glucose starvation

(Fig. 2F and Figure S2I). Additionally, UOK262 cells were tested in different durations of glucose starvation, followed by activation of intracellular caspases using STS. The results showed that overexpression of FH in UOK262 cells led to Caspase-3 activation regardless of the starvation duration (Red arrow) (Fig. 2G). However, in vector control UOK262 cells, Caspase-3 dimerization was observed (Fig. 2G, green arrow), and the cleaved Caspase-3 was significantly inhibited (Fig. 2G, red arrow). These results show that glucose starvation quickly inactivates caspases in $FH^{deficient}$ cells, suggesting an alternative form of cell death triggered by disulfide accumulation.

Metabolomic analysis of disulfide stress in FH Cells

To clarify the impact of FH deficiency on the PPP, we labeled UOK262 cells with U-$^{13}C_6$-glucose. We found that, compared to FH-overexpressing UOK262 cells, there were no significant changes in M + 6 glucose-6-phosphate (G6P) and M + 5 ribulose-5-phosphate (Ru5P) (Figure S3A), suggesting that FH deficiency did not cause a change in the PPP flux. However, Ribose-5-phosphate (R5P) was significantly elevated in $FH^{deficient}$ UOK262 compared to FH-overexpressing UOK262 cells. R5P is involved in subsequent nucleic acid synthesis[21], indicating that $FH^{deficient}$ cells are more reliant on the PPP to generate R5P for nucleic acid production under glucose conditions. Additionally, FH-overexpression significantly reduced fumarate levels in UOK262 cells and led to increased intracellular GSH levels (Figure S3B). Fumarate succinates GSH through fumarate-cysteine adducts (Figure S3C), leading to its degradation[22,23]. To clarify whether high levels of fumarate could promote cell death under glucose starvation, accumulation of fumarate was driven by FH-IN1 for various durations, followed by cell survival analysis (Figure S3D). We found that with prolonged FH-IN1 treatment, cells with higher fumarate levels died more rapidly under glucose starvation (Figure S3D). Moreover, under the same duration of glucose starvation, cells with higher fumarate levels exhibited more pronounced actin cytoskeleton-associated proteins aggregation (Figure S3E). Therefore, elevated fumarate levels in $FH^{deficient}$ cells lead to GSH inactivation, causing oxidative stress and making the cells more dependent on the reductive power provided by the PPP. Additionally, we measured intracellular ROS levels and found that, unlike the disulfide stress mediated by high expression of SLC7A11, ROS levels were significantly reduced in FH-knockdown 786-O cells under glucose starvation (Figure S3F). This also suggested that NAD(P)H, as an electron donor, may be depleted in $FH^{deficient}$ cells under glucose starvation. Metabolic analysis revealed significant alterations in the TCA cycle and nicotinate and nicotinamide metabolism in FH^{Inact} HeLa cells under glucose starvation (Figure S3G and S3H). Further investigation of NAD(H) and NADP(H) levels showed that glucose-starved FH^{Inact} HeLa/MCF-7 cells and $FH^{deficient}$ UOK262 cells exhibited substantial down-regulation of both NAD(H) and NADP(H) (S3I and S3J). Therefore, under glucose starvation, FH deficiency disrupted the oxidative TCA cycle, leading to the impairment of nicotinate and nicotinamide metabolism.

To explore the metabolic mechanisms behind disulfide stress, we performed quantitative proteomic analysis on $FH^{deficient}$ UOK262 cells under glucose-containing and glucose-free conditions. The results

showed minimal protein changes due to glucose starvation (Fig. 3A). However, at the metabolic level, all metabolites, except glutamine and glutamate, were reduced to varying degrees in the glucose-free group (Fig. 3B). These findings suggested that it could be due to the regulation of metabolism rather than quantitative levels of metabolic enzymes. Compared to glucose, $FH^{deficient}$ cells are more reliant on glutamine, using the reductive TCA cycle to synthesize macromolecules that support cell growth[24]. However, the reductive TCA cycle often requires NADPH to drive its reactions[25,26]. Therefore, we labeled $FH^{deficient}$ UOK262 cells with U-$^{13}C_5$-glutamine under both glucose-containing and glucose-free conditions to clarify the operation of the TCA cycle in $FH^{deficient}$ cells. In M + 5 glutamine-labeled cells, the reductive TCA branch involved the conversion of M + 5 α-ketoglutarate (α-KG) to M + 5 citrate, with NADPH providing the reductive power. This was further converted into M + 3 oxaloacetate, and ultimately into M + 3 malate and aspartate. In contrast, the oxidative branch involved the conversion of M + 5 α-KG into M + 4 succinate, M + 4 fumarate, and M + 4 malate (Fig. 3C). The results showed that in the oxidative branch, M + 3 succinate, M + 4 malate, and M + 4 aspartate all significantly increased, while in the reductive branch, M + 3 malate and M + 3 aspartate significantly decreased (Fig. 3D). This suggested that $FH^{deficient}$ cells reprogrammed their metabolism to enhance the oxidative TCA cycle and reduce the reductive TCA cycle to mitigate the effects of glucose starvation.

JX06, a pyruvate dehydrogenase kinase (PDK) inhibitor, could promote the entry of pyruvate into the TCA cycle to enhance the oxidative TCA cycle (Figure S3K). JX06 inhibition of FH^{Inact} HeLa cells illustrated cell death under glucose starvation (Figure S3L), due to its effect on reducing pyruvate and increasing downstream products and NADP(H) (Figure S3M). We hypothesized that under glucose starvation, $FH^{deficient}$ cells enhanced the conversion of aspartate to the oxidative TCA cycle (malate-aspartate shuttle) to compensate for the defects in the oxidative TCA cycle. To investigate this, we used U-$^{13}C_4$-aspartate labeled cells to analyze aspartate metabolism (Fig. 3E). The results showed that under glucose starvation, $FH^{deficient}$ UOK262 cells exhibited a significant increase in the fraction of M + 4 aspartate, M + 4 malate and M + 3 α-KG (Fig. 3F). The M + 4 malate/M + 4 aspartate ratio was significantly elevated (Fig. 3G). These findings suggested that $FH^{deficient}$ cells enhance the utilization of aspartate under glucose starvation, converting it to malate to support the oxidative TCA cycle. We also observed that $FH^{deficient}$ UOK262 cells showed reduced succinate oxidation compared to FH-overexpressing UOK262, as evidenced by the significantly decreased ratio of M + 2 fumarate to M + 2 succinate (Fig. 3H). Subsequently, further analysis of TCA cycle metabolites following aspartate supplementation revealed increased fumarate levels and a significant rise in the fumarate-to-succinate ratio (Fig. 3I and 3J). Additionally, aspartate supplementation upregulated the GSH/GSSG ratio and NADPH production and reduced the proportion of cell death (Fig. 3K, 3L and 3M). This part of the results suggested that, although $FH^{deficient}$ cells compensated for NADPH deficiency under glucose starvation by enhancing aspartate utilization and reducing the reductive TCA cycle, FH deficiency led to defects in the oxidative TCA cycle and high fumarate levels, which impaired GSH consumption, ultimately causing the depletion of reducing agents and triggering disulfide stress under glucose starvation.

To further investigate tumor suppression *in vivo*, mice were randomized to a normal diet (glucose normal, GN) or a ketogenic diet (glucose deprived, GD) after tumor injection. Intraperitoneal injections of FH-IN1 (FH inhibitor) were administered every 3 days at a dose of 10 mg/kg (Figure S4A). Random blood glucose samples from mice revealed that the blood glucose levels in the GD group were significantly lower than those in the GN group, as expected (Figure S4B). GN and GD mice were injected with tumorous cells subrenally to mimic FH deficient RCC. However, in contrast to GD and GN group, tumor proliferation in the FH-IN1/GD group was significantly inhibited (Figures S4C). Subsequent tumor slices revealed numerous necrotic areas (white line) in the GD and GD/FH-IN1 groups, the ratio of cell death areas was significantly increased than that GN groups tumors (Figure S4D). To reveal metabolic changes after tumor suppression with FH inhibition, we analyzed the metabolic profiles of tumor tissues in these two groups (GD, GD/FH-IN1). At a cellular level, we assessed differences in cellular metabolism between the dead region (D) versus the tumor region (T) within the GD/FH-IN1 group by mass spectrometry imaging (MSI), and laser capture microdissection-based gas chromatography-mass spectrometry/multi-reaction monitoring (LC-GC/MRM MS) (Figure S4E). As shown in the MSI results, both the D region of GD and GD/FHIN1 groups showed low levels of GSH than the T regions (Figure S4F). This indicated a breakdown of the reductive equilibrium in the D region. We analyzed the TCA metabolites in the T region of both GD and GD/FH-IN1 groups using LCM-GC/MRM MS. The results showed that the metabolites involved in TCA cycle in the GD/FH-IN1 group were globally decreased (Figure S4G). We then analyzed F-actin staining in the D and T regions, in which F-actin aggregation was significantly upregulated in the D region in GD/FH-IN1 group, but not in the D region of GD group (Figure S4H). Therefore, these results suggested glucose deprivation could mediate disulfide stress in FH-inactivated tumors and thus inhibit tumor growth.

Targeting mitochondrial complexes with Rotenone and Antimycin A promotes disulfide-induced cell death in FH cells

Glucose starvation-induced cell death in $FH^{deficient}$ cells occurs slowly (> 10 hours). Therefore, we sought to identify synthetic lethal targets that could have applications on promoting disulfide stress as a therapeutic strategy for $FH^{deficient}$ RCC. By screening a small molecule compound library targeting 200 metabolic targets under glucose starvation (Table S2), we identified the top ten compounds that significantly promoted cell death (Table S3), five of them were involved in the mitochondrial oxidative phosphorylation process (Rotenone, Fenofibrate, Fipronil, Antimycin A, and Gboxin) (Fig. 4A). Among these, we selected Rotenone and Antimycin A, both of which specifically target mitochondrial ETC complex, for further investigation, we assessed cell death using colony formation assays with Rotenone and Antimycin A, both in the presence and absence of glucose. The results indicated that, targeting mitochondrial complexes I and III significantly promoted cell death under glucose starvation (Fig. 4B and 4C). The inhibition of these complexes heightened disulfide stress in $FH^{deficient}$ cell under glucose starvation (Fig. 4D and 4E). By detecting TCA cycle metabolites, we found that suppression of Complexes I (Rotenone treatment) and III (Antimycin A treatment) resulted in a increase of glutamate

and reduction of □-KG, fumarate, malate, GSH under glucose starvation (Fig. 4F). In $FH^{deficient}$ UOK262 cells, inhibition of complexes I and III further decreased the succinate oxidation (Fig. 4H) and reduced NAD(H) and NADPH levels under glucose starvation (Fig. 4F and 4G). These results suggested that targeting mitochondrial complexes in $FH^{deficient}$ cells further disrupted NADPH balance. Next, $FH^{deficient}$ UOK262 cells were labeled with U-$^{13}C_5$-glutamine while blocking ETC activity under glucose starvation. The results indicated that, compared to the control group, the inhibition of complexes I and III led to an increased M + 5 glutamate and □-KG fraction, while led to a decreased M + 4 fumarate fraction (Fig. 4J). Meanwhile, we examined the NADPH-consuming reductive TCA branch by assessing the ratio of M + 3 malate (reductive TCA branch) to M + 4 malate (oxidative TCA branch). Our findings demonstrated that the inhibition of complexes I and III significantly elevates the ratio of M + 3 malate to M + 4 malate under glucose starvation (Fig. 4K). Therefore, complex I and III inhibition increased the reductive TCA branch and further decreased succinate oxidation in $FH^{deficient}$ cells under glucose starvation (Fig. 4O). Collectively, these findings suggested ETC impedance caused impairment of oxidized TCA branch and enhanced $FH^{deficient}$ cell disulfide stress under glucose starvation.

Targeting Complex I with Metformin induces disulfide stress in $FH^{deficient}$ RCC cells under concurrent low-glucose conditions

Metformin has a dual capability of lowering blood glucose levels while also targeting mitochondrial complex I[27]. Therefore, we further investigated the effect of metformin targeting complex I on cell death under physiological blood glucose (5 mM) concentrations. Under 5 mM glucose conditions, the proportion of cell death in $FH^{deficient}$ UOK262 cells significantly increased with prolonged metformin treatment (Fig. 5A). Similarly, HeLa cells with FH-IN1 treatment combined with metformin also exhibited markedly increased cell death under 5 mM glucose (Figure S4I). Subsequently, $FH^{deficient}$ UOK262 cells were treated with various cell death inhibitors. The results revealed that inhibitors of apoptosis (Z-VAD), necroptosis (NEC-1), and ferroptosis (Ferr-1) were ineffective in preventing metformin-induced cell death (Figure S4J and Fig. 5B). Immunofluorescence analysis revealed that ROS scavenger Troxol and Temple could not rescue metformin-mediated F-actin aggregation, whereas TCEP was able to inhibit F-actin aggregation (Fig. 5C). Meanwhile, metformin markedly decreased intracellular levels of NAD(H) and NADP(H) (Fig. 5D and 5E). Non-reducing and reducing immunoblot analysis demonstrated that metformin promoted actin cytoskeletal-associated protein polymerization (FLNA, Drebrin) and caspase-3 dimerization in $FH^{deficient}$ UOK262 cells (Fig. 5F). Therefore, these results suggested that metformin can induce disulfide stress in $FH^{deficient}$ cells under physiological blood glucose (5 mM) concentrations.

To analyze the effects of metformin on intracellular PPP, glycolysis, and TCA cycle flux, we utilized different concentrations of U-$^{13}C_6$-glucose to label $FH^{deficient}$ UOK262 cells (Fig. 5G). The results showed that as the concentration of U-$^{13}C_6$-glucose decreased, the fraction of M + 3 3-phosphoglycerate (3PG) and phosphoenolpyruvate (PEP) (glycolysis) and M + 5 Ru5p and R5P all gradually reduced. In comparison to the control group (H_2O), metformin exhibited no significant impact on the fraction of M +

5 Ru5p and M + 5 R5P. However, metformin significantly reduced the M + 2 fumarate and M + 2 succinate fractions (Fig. 5H and 5I), indicating that metformin can markedly inhibit the flux of glucose into the TCA cycle. With $FH^{deficient}$ UOK262 cells labeled with the U-$^{13}C_5$-glutamine under 5 mM glucose, we found metformin increased the fraction of M + 5 □-KG and M + 4 succinate and decreased the fraction of M + 4 fumarate (Fig. 5J). This finding implied that metformin further inhibited succinate oxidation in $FH^{deficient}$ UOK262 cells. In the studies with $FH^{deficient}$ UOK262 cells labeled with U-$^{13}C_5$-glutamine over varying time intervals under 5 mM glucose, the results showed that the M + 4 succinate-to-M + 4 fumarate ratio in the control group (H_2O) gradually increased over time and no significant change in the metformin treated group over the time period. Specifically, the M + 4 fumarate-to-M + 4 succinate ratio was notably lower in the metformin group compared to the control group after 2.5 hours of drug treatment (Fig. 5K). These findings suggest that metformin significantly inhibits succinate oxidation under low glucose conditions. As previously mentioned, inhibition of complex I or III results in an increase in the reductive TCA cycle flux. We also measured changes in the reductive TCA flux using the ratio of M + 3 malate to M + 4 malate and the results showed that with the extension of the labeling time, the ratio of M + 3 malate to M + 4 malate in the metformin group significantly increased over time (Fig. 5L). Therefore, these results indicated that under low glucose conditions, metformin enhanced the reductive TCA cycle branch and reduced glucose flux into the TCA cycle, thereby inhibiting the oxidative TCA cycle branch. This ultimately led to NAD(P)H metabolic dysregulation and induced disulfide stress-cell death in $FH^{deficient}$ cells (Fig. 5M).

Targeting Complex I with metformin inhibits FH tumor growth

Next, we aimed to investigate whether metformin could inhibit the growth of $FH^{deficient}$ tumors. We used luciferase-labeled $FH^{deficient}$ UOK262 cells to implant tumors into the subrenal capsule in mice and grouped them based on similar tumor fluorescence intensity. Considering the fluctuating effects of metformin on blood glucose[27], we did not use a ketogenic diet but instead employed intermittent fasting as a control to lower blood glucose in mice. As illustrated in Fig. 6A, the treatment protocol involved feeding the mice a normal diet while administering either a solvent (Fed/Vehicle) or metformin (Fed/Met), following previously reported conditions[28]. Additionally, some mice were subjected to a 24-hour fasting period followed by a 24-hour feeding period, during which they received either a blank solvent (Fasting/Vehicle) or metformin (Fasting/Met) via gavage. This treatment cycle was maintained for 48 hours. Monitoring of the blood glucose levels of mice in the morning and late stages revealed that the Fed/Met, Fasting/Vehicle, and Fasting/Met groups successfully reduced blood glucose levels to below 5 mM (Fig. 6B). Subsequent *in vivo* imaging indicated that the tumor growth in the metformin-treated groups (Fed/Met, Fasting/Met) was nearly halted (Fig. 6C and Fig. 6D). Given the dependence of FH deficient cells on glutamine as an energy sources, we injected glutamine into the tail vein of the mice and performed metabolomic analysis on the isolated implanted renal tumors (Fig. 6E). Consistent with the cellular findings, the metformin treated group exhibited a decrease in the ratio of M + 4 fumarate to M + 4 succinate, while Fasting/Met further decreased the ratio of M + 4 fumarate to M + 4 succinate

compared to Fed/Met group (Fig. 6F). Additionally, the metformin treated group showed a significant increase in the ratio of M + 3 malate to M + 4 malate (Fig. 6G). Further analysis revealed that the GSH and NADH levels were significantly reduced in the Fed/Met and Fasting/Met groups (Fig. 6H), and that the actin cytoskeleton-related proteins (FLNA, Drebrin) and Caspase-9 underwent polymerization (Fig. 6I). These results suggested that metformin can inhibit $FH^{deficient}$ tumor proliferation by reducing circulating glucose levels, enhancing the reductive TCA branch and suppressing succinate oxidation.

Discussion

In this study, we identified a form of disulfide stress-induced cell death by FH deficiency under glucose starvation (Figure S6A). FH deficiency disrupts the TCA cycle, also affecting NADPH-producing pathways such as isocitrate-□-KG and malate-pyruvate[29]. Additionally, in $FH^{deficient}$ cells, reduced glucose utilization by the TCA cycle and elevated fumarate levels promotes the succination of GSH[22,23,30], leading to a severe reliance on the PPP for NADPH production to counteract cellular disulfide stress. We found that FH deficiency under glucose starvation conditions compensates for NADPH depletion by enhancing the oxidative TCA cycle through increased aspartate and glucatmine utilization and reducing the NADPH-consuming reductive TCA cycle branch (glutamine-□-KG-malate branch). However, defects in the oxidative TCA cycle prevent $FH^{deficient}$ cells from maintaining nicotinate and nicotinamide metabolism balance under glucose starvation (Figure S6A). Compound library screening also revealed that inhibition of NAD + biosynthesis (Daporinad targeting NMPRTase) promotes cell death (Fig. 4A). Taken together, $FH^{deficient}$ cells are unable to maintain normal NAD(P)H metabolism under glucose starvation, leading to the excessive accumulation of disulfides.

Compared to glucose starvation induced disulfide stress in $SLC7A11^{high}$ cells (termed disulfidptosis)[7], $FH^{deficient}$ cells and $SLC7A11^{high}$ cells share about 58 common proteins, with 21 of these proteins related to cell adhesion and the actin-cytoskeleton associated protein (Figure S6B and S6C). Under glucose starvation, cysteine-containing peptide chains in $FH^{deficient}$ cells are more likely to form disulfide bonds at the CxR sequence (Figure S6D), which is different from cells with high expression of SLC7A11[7]. One possible reason is that the high levels of fumarate in $FH^{deficient}$ cells can directly succinate cysteine residues[31], leading to a bias in the formation of disulfide bonds in certain proteins. Additionally, under glucose starvation, $FH^{deficient}$ cells experience NAD(P)H depletion driven by mitochondria, leading to a differential accumulation of disulfide proteins in the cytoplasm compared to $SLC7A11^{high}$ cells (Figure S6E and S6F). In $SLC7A11^{high}$ cells, Rac regulates the formation of lamellipodia, leading to actin cytoskeleton branching through Arp2/3. The resulting scattered actin cytoskeleton is more susceptible to disulfide stress[7]. We found that the contractile force generated by actin-myosin filaments, formed through the interaction of myosin and actin regulated by ROCK, plays a role in driving cell death induced by disulfide stress. An important feature of disulfide stress-induced cell death is the crosslinking of myosin and actin via disulfide bonds[7,32]. This enhanced crosslinking may lead to a sustained increase in the contractile force of the actin cytoskeleton, ultimately triggering the separation of the actin

cytoskeleton from the plasma membrane and resulting in cell death. This explains why the separation of the actin cytoskeleton from the plasma membrane is observed in both $FH^{deficient}$ and $SLC7A11^{high}$ cells.

Importantly, we have unraveled that caspases in $FH^{deficient}$ cells aggregate through disulfide bonds under glucose starvation, which ultimately leads to their inactivation. This suggests that $FH^{deficient}$ RCC may utilize this mechanism to make the tumors resistant to therapies that target those pathways. One method to inhibit tumor growth is to restrict glucose uptake through methods such as a ketogenic diet or intermittent fasting, which accelerates disulfide stress in $FH^{deficient}$ cells. However, it remains uncertain whether this approach is effective for $SLC7A11^{high}$ tumors. One of the key reasons for the poor survival rates in patients with $FH^{deficient}$ RCC is its high tendency for distal metastasis[33]. Complex I plays a crucial role in renal cancer metastasis: Stimulating respiration or NADH recycling in kidney cancer cells is sufficient to promote metastasis, while inhibiting Complex I reduces metastasis[34]. Metformin, by lowering blood glucose levels and targeting Complex I, induces abnormal disulfide accumulation and inhibits tumor growth in $FH^{deficient}$ RCC. Therefore, complex I inhibitors currently in clinical trials, like IACS-010759[35,36], when used in combination with blood glucose control, may provide an effective therapeutic approach for $FH^{deficient}$ tumors.

Materials and Methods

Cell culture and treatment

All cell lines used in this study were cultured at 37°Cin 5% CO_2 in a humidified incubator. UOK262, 786-O, HeLa, MCF-7 and HEK293T were maintained in Dulbecco's modified Eagle's medium (DMEM, GIBCO, C11995500BT) or RPMI-1640 medium (GIBCO, C11875500BT) containing 10% fetal bovine serum (NEWZERUM, FBS-UY500) and 1% penicillin-streptomycin double antibody. For glucose starvation cultivation, UOK262 (Empty vector), UOK262 (FH-overexpression), 786-O (Empty vector), 786-O (SLC7A11-overexpression), 786-O (FH-knockdown) were cultured in glucose-free RPMI-1640 medium (Pricella, PM150122) containing 10% fetal bovine serum and 1% penicillin-streptomycin double antibody for the indicated times. For isotope labeling experiment, cells were cultured in 2 mM L-$^{13}C_5$-Glutamine (CIL, Cat#: PR-30230; CAS#:184161-19-1), 20 mM L-$^{13}C_4$-Aspartate (CIL, Cat#:PR-33918; CAS#:55443-54-4) or indicated concentrations of D-$^{13}C_6$-Glucose (CIL, Cat#:PR-30820; CAS#:110187-42-3) culture medium for the indicated times.

In vivo animal studies

Immunodeficient NYG mice (4–6 weeks old) were injected into the flank with 5×10^6 HeLa cells. After two weeks, mice with the same tumor size were randomly divided into four groups. Mice were fed a ketogenic diet (Table S4) or general diet for 3 days. Afterwards, mice were injected intraperitoneally with 10 mg/kg of FH-IN1 or blank solvent (10% DMSO + 90% corn oil) every 3 days. Tumor size was measured with vernier calipers before the mice were injected (tumor volume was calculated by formula V=

(L×W2)/2, V: tumor volume, L: tumor long diameter, W: tumor short diameter). After completing five consecutive injections to 18 days, the mice were euthanized, and the tumors and major organ tissues were snap frozen.

UOK262-Luc cells were cultured until they reached the logarithmic growth phase. After trypsinization, the cells were injected nto the left supcapsular kidney of 8-week-old female nude mice (from GemPharmatech Co., Ltd, Jiangsu, China). Bioluminescence imaging was conducted every two days to monitor tumor growth. Mice with similar fluorescence intensity and a consistent growth trend were randomly assigned to one of four groups (8 mice in each group). Vehicle refers to administering a blank solvent by gavage to the mice at 9:00 AM, while metformin (Met) is administered by gavage at a dose of 200 mg/kg at 9:00 AM. The groups were as follows: one group received normal feeding and 200 mg/kg of metformin via oral gavage, while another group received normal feeding and an equal volume of water. The third group fasted for 24 hours (water only) and then resumed normal feeding, with 200 mg/kg of metformin hydrochloride (Shandong Sparkjade Biotechnology Co., Ltd) administered during the fasting period. The fourth group fasted for 24 hours (water only) and then resumed normal feeding, with an equal volume of water given during the fasting period. Before administering metformin, measurements for the mice were recorded as "0." Subsequent treatment cycles were labeled as "1st ," "2nd ," and so forth. Each treatment cycle lasted two days, during which imaging and blood collection were performed. The experiment was concluded when tumors in one of the groups had nearly disappeared. Three mice from each group were selected for two tail vein injections of 0.2 M L-$^{13}C_5$-Glutamine, administered every 15 minutes. Following this, the kidneys were collected and immediately snap-frozen in liquid nitrogen for subsequent analysis. The use of animals was approved by the Institutional Review Board of Nanjing Medical University (Nanjing, China).

Redox Proteomics

Glucose starved-786-O and UOK262 cells were dissolved with 200 µL lysis buffer (4% SDS, 150 mM Tris-HCl pH 8.0). Protein (4 mg) from each sample was precipitated with pre-cooled acetone and the free cysteines of proteins were blocked by mixing for 12 h at 4℃ in 5 mL total PBS containing 0.5% SDS, 1% Triton X-100 (Sigma-Aldrich), protease inhibitors (Thermo Scientific), 5 mM EDTA and 25 mM NEM (N-ethylmaleimide, Thermo Scientific). Samples were precipitated using chloroform/methanol to remove excess NEM. Proteins were resuspended in 2SB buffer (50 mM Tris-HCl, 2% SDS, 5 mM EDTA, pH7.4), mixed with the same volume of 50 mM DTDP (in DMSO) and incubated at RT for 1 h and the extra DTDP were precipitated with chloroform/methanol or acetone. Proteins were resuspended in 4% SDS in PBS buffer, and then divided into two equal parts, one was mixed with 10 mM DTT to reduce all disulfide bonds, and the other was added with the same amount of the corresponding buffer for control, then incubated with 200 µL of 27.5 mM EDTA in PBS buffer, and 100 µL of 4 mM Biotin-HPDP in DMSO for 3 h with gentle mixing. Proteins were precipitated again and resuspended in 6 M urea and diluted 6 folds with 50 mM ammonium bicarbonate, and then digested with trypsin at the enzyme-to-protein ratio of 1:50 into the sample and incubated at 37℃ for 20 h. The trypsin digested peptides were first desalted with a C18 spin column (Thermo Scientific). The dried peptides were resuspended with 200 µL loading

buffer (0.2% SDS, 0.2% Triton X-100 and 500 mM NaCl) and mixed with 100 µL of high-capacity streptavidin beads (Thermo Scientific) for 2 h at room temperature. Beads were washed three times with 5 mL PBS containing 0.2% SDS, 0.2% Triton X-100 and 500 mM NaCl and then collected after washing with PBS twice. The beads were then incubated with 0.2 mL elution buffer (50 mM NH_4HCO_3, 10 mM TCEP) for 2 h at room temperature. The eluted peptides were collected and mixed with 50 mM iodoacetamide to block reduced cysteine residues, which indicated the S-oxidation sites. Finally, the peptides were desalted with C18 StageTips and prepared for further LC-MS/MS analysis.

LC-MS/MS were performed on an Orbitrap Astral mass spectrometer coupled with a Vanquish Neo UHPLC system (Thermo Fisher Scientific). Peptides from each sample were loaded into a column (50 cm Low-Load µPAC™ Neo HPLC Column Thermo Scientific) at a flow rate of 2.2 µL/min. The RP – HPLC mobile phase A was 0.1% formic acid in water, and B was 0.1% formic acid in 80% acetonitrile. Peptides were eluted over 8 min with a linear gradient of buffer B at 1.25 µL/min. The linear gradient was set as follows: 0-0.1 min, linear gradient from 4–6% buffer B; 0.1–1.1 min, linear gradient from 6–12% buffer B; 1-4.3 min, linear gradient from 12–25% buffer B; 4.3–6.1 min, linear gradient from 25–45% buffer B; 6.1–6.5 min, linear gradient from 45–99% buffer B; 6.5-8 min, buffer B maintained at 99%. The eluted peptides were analyzed on an Orbitrap Astral mass spectrometer. The DIA method consisted of a survey scan from 380–980 m/z at resolution 240,000 with AGC target of 500% and 5ms injection time. The DIA MS/MS scans were acquired by Astral from 150-2,000 m/z with 2 m/z isolation window and with AGC target of 500% and 3ms injection time. Normalized collision energy was set 25 and cycle time was 0.6s. The spectra of full MS scan and DIA scan were recorded in profile and centroid type respectively.

The DIA MS data were analyzed using Spectronaut 18 (Biognosys AG, Switzerland). MS data were searched against the UniProtKB database (uniprotkb-Homo sapiens (Human) [9606]-204141020240326. fast. 204141 total entries). Tryptic cleavage specificity was applied, along with variable methionine oxidation (M), variable protein N-terminal acetylation, variable N-ethylmaleimide (C) and Carbamidomethylation (C). The minimum 6 amino acids for peptide and at least 1 unique peptide were required per protein. For peptide and protein identification, the false discovery rate (FDR) was set to 1%. Site quantitation analysis was filtered only for those carbamidomethylated cysteine sites that were confidently localized > = 0.75 site probability with the algorithm. Label-free quantification was carried out using intensity determination. The quantitative site ratios were weighted and normalized by the median ratio. Bioinformatic data analysis was carried out with Perseus software, Microsoft Excel, Python and R statistical computing software. K-Nearest Neighbors (KNN) algorithm was used for imputing missing values and resampling datasets. Differentially significant expressed sites were screened with the cutoff fold-change ratio of > 2 or < 0.5 and P-values < 0.05. Expression data were grouped together by hierarchical clustering according to the site level, which is based on the open-source statistical language R25, using Euclidean distance as the distance metric and complete method as the agglomeration method. To annotate the sequences, information was extracted from UniProtKB/Swiss-Prot, Kyoto Encyclopedia of Genes and Genomes (KEGG), and Gene Ontology (GO). GO and KEGG enrichment analyses were carried out with Fisher's exact test, and FDR correction for multiple testing was also performed. GO terms were grouped into three categories: biological process (BP), molecular function

(MF), and cellular component (CC). Enriched GO and KEGG pathways were nominally statistically significant at the $p < 0.05$ level. The construction of protein-protein interaction (PPI) networks was also conducted using the STRING database with the Cytoscape software. The statistically significant enriched phosphorylation motifs of kinase-substrates were discovered by the MOMO software.

Transmission Electron Microscope (TEM) staining

10 cm-dish cells were harvested and fixed with 4% paraformaldehyde overnight at 4℃. Cells were prefixed with 1% OsO_4 in 0.1 M PBS (pH 7.4) for 2 h at room temperature. After OsO_4 removal, cells were washed 3 times for 15 min each with 0.1 M PBS (pH 7.4). Dehydration with ethanol uptitration at room temperature: 30%, 50%, 70%, 80%, and 95% ethanol for 20 min. 100% ethanol wash twice, 20 min each, followed by acetone treatment twice for 15 min. The infiltrating resin deposition method was as follows. Acetone: EMBed 812 = 1:1, soak at 37°C for 2–4 h. Acetone: EMBed 812 = 1:2, overnight at 37°C. Clean EMBed812 implants at 37°C for 5–8 h. Cast the whole EMBed812 embedding template, place the tissue in the whole EMBed812 and baked at 37°C overnight. The resin-embedded models and samples were polymerized in a 65°C oven for more than 48 h. The resin block was then removed from the embedding model and stored at room temperature for later use.

The resin block was cut into a thickness of 60–80 nm on an ultra-microtome, and the tissue was isolated using a 150-mesh copper grid covered with Formvar foil. Next, tissues were stained with 2% saturated uranyl acetate solution in the dark for 8 min, rinsed 3 times with 70% ethanol, and rinsed 3 times with ultrapure water. The samples were stained with 2.6% lead citrate for 8 minutes, avoiding CO_2 exposure, and washed 3 times with ultrapure water. After drying on filter paper, the copper grids were placed on grid plates and dried overnight at room temperature. Finally, the copper grids were observed under TEM, and images were acquired.

GC-MS based metabolomics analysis and metabolic flux analysis.

For tissue preparation, each mouse tissue was cut approximately 15 mg and mixed with 900 µL of cold extractant (80% methanol in water containing 5 µg/ml tridecanoic acid as internal standard). The cells were sonicated for 30 min at 30 kHz, 4°C. After centrifugation at 15,000 g for 10 min at 4°C, 600 µl of supernatant was collected to lyophilize using Labconco vacuum concentrators.

For cell preparation, cells were washed three times rapidly with ice-cold PBS. Then 1 mL of cold methanol (4°C) was added to cell pellets rapidly to quench metabolism and the cells were scraped off and transferred to a 2 mL tube. The mixture was vortexed for 30 seconds and then homogenized at 30 Hz for 30 s twice. The mixture was centrifugated at 15,000 g for 10 min at 4°C, and 700 µL of supernatant was collected for lyophilization.

For derivatization of mouse tissue, 50 µL methoxyamine-pyridine solution (20 mg/ml) was added to resuspend the powder and the oxime reaction was kept at 37°C for 1.5 h. Afterwards, 40 µL of N-Methyl-N-triMethylsilyl) trifluoroacetamide (MSTFA, Sigma-Aldrich, St. Louis, USA) was added for a silylation

reaction at 37°C for 1 h. The reactant was centrifuged, and a volume of 1 μL. The supernatant was analyzed by GCMS-QP2010 Plus (Shimadzu, Japan) using a DB-5MS column (30 m × 0.25 mm × 0.25 μm, Agilent Technologies). The flow rate of the carrier gas (helium) was set to 1 mL/min and the column temperature was maintained at 80°C for the first 1 min, then increased to 210°C at 30°C/min, then to 320°C at 20°C/min and kept for 4 min. Quality control (QC) samples were inserted every 10 samples during the analytical batch. Identification of metabolites was based on standard commercial libraries (NIST, USA) and a home-made metabolite library. The split ratio was set at 40:1, and the temperature of ion source was 230°C.

The isotope-labeled intercellular metabolites extraction was performed with the same protocol described above for cultured cell preparation for GC-MS. A volume of 40 μL methoxyamine–pyridine solution (20 mg/ml) was added to the resuspended sample and an oxime reaction was maintained at 37°C for 1.5 h, then 40 μL N-tert-Butyldimethylsilyl-N-methyltrifluoroacetamide (MTBSTFA, Sigma-Aldrich, St. Louis, USA) with 1% tert-Butyldimethylchlorosilane was added for a silylation reaction at 55°C for 1 h. The reactant was centrifuged, and the supernatant was analyzed by GCMS-QP2010 Plus (Shimadzu, Japan) using a DB-5MS column (30 m × 0.25 mm × 0.25 μm; Agilent Technologies). A volume of 1 μL was injected in the splitless mode for each sample. The column temperature was maintained at 100°C for 3 min, then increased to 310°C at 3.5°C/min, and kept for 5 min. Identification of isotope-labeled metabolites was based on an internal metabolite library (based on an in-house library built with authentic standard compounds). Raw isotopic data were imported into Stable Isotope-Assisted Metabolomics Analyzer (SIAMA) to perform data filtering.

MALDI-FTICR-MSI measurement

The mouse tumor was stored at -80°C before sample preparation. The tissue was fixed on the sample holder and cryosectioned at a thickness of 10 μm using Leica CM1950. A parallel tissue section was stained by cresyl violet acetate (Sigma-Aldrich, St. Louis, USA). Then the tissue section was thaw-mounted onto the ITO-coated glass slide and desiccated at room temperature before matrix application. The matrix solution containing 10 mg/mL N-(1-naphthyl) ethylenediamine dihydrochloride monomethanolate (Sigma-Aldrich, St. Louis, USA) in 70% methanol/deionized water was sprayed on the section by iMlayer Aero (Shimazu, Japan) with 27 layers. The working table speed and the spray distance were set at 6 cm and 20 s. The drying time was set at 75 mm/s. The frequency for washing the nozzle was set at 1 layer per wash.

MALDI-FTICR-MSI was performed on a SolariX XR-15T FTMS (BrukerDaltonicsGmbH, Bremen, Germany) at m/z range of 92–600 in negative ionization mode with a 1 M data point transient, using 1,000 laser shots and 100 μm pixel size. The instrument was calibrated with NaTFA before analysis. Visualizations were performed by flexImaging 5.0 (Bruker Daltonics).

Laser Capture Microdissection (LCM)-GC-MS analysis

The slides were placed below the slides to make a sandwich. The sandwich was placed on top of the microscope. The slide was scanned using a 4x objective to achieve an overview of the entire slide. The

20x lens was chosen and parameters were adjusted to the following: laser energy (60% power), focus and cutting speed (10 μm/s). Excised cells were collected using IsolationCaps (MMI). To extract the metabolites, 50 μL of methanol/H_2O/FA (5:4:1) was added into the vial, which was further inverted and sonicated at 4°C at 100 Hz for 30 min. Then, the mixture was centrifuged at 14,000 g for 15 min and the supernatant was isolated and dried with a rotating freeze-dryer. For derivatization, 3.5 μL of methoxyamine solution (20 mg/mL in pyridine) and vortexed for 5 min. The mixture was then incubated at 37°C for 2h. Then, 1 μL of N-methyl-N-(trimethylsilyl)-trifluoroacetaminde was added to the mixture followed by incubation at 37°C for 1h. After 14,000 g centrifugation for 15 min, 1 μL of the supernatant was used for GC/MRM analysis.

LC-MS based metabolomics and metabolic flux analysis.

The pre-treatment of cells for metabolomics and metabolic flux analysis was performed as follows. After removing the medium, the cells were washed three times with PBS. Next, cell culture dishes were subjected to liquid nitrogen for 1 min for cell quenching. Then, 200 μL of 80% methanol (v/v) aqueous was added to the cells, after which the cell suspension was harvested. The operation was repeated and each resultant suspension was combined. After being centrifuged at 12000 g for 15 min, 350 μL of the supernatant was isolated and dried by rotation vacuum. Before sample analysis, 40 μL of 50% methanol (v/v) aqueous was added to the residue and vortexed at 8°C for 5 minutes. The supernatant after centrifugation was transferred to the sampling vial.

Sample analysis was performed according to the method of Agilent Pathway-Directed Metabolomics and Flux Analysis (Agilent, Santa Clara, USA). In detail, chromatographic separation was conducted using a 1290 series ultra-performance liquid chromatography system (Agilent, Santa Clara, USA) with a BEH amide column (2.1 mm × 100 mm, 1.7 μm, (Waters, Milford, MA)). The organic phase (B) was the 90% acetonitrile (v/v) aqueous with 15 mM ammonium acetate and 0.3% ammonium hydroxide, and the aqueous phase was the de-ionized water with 15mM ammonium acetate and 0.3% ammonium hydroxide. The flow rate was 0.3 mL/min and the column temperature was 40°C. The gradient was used as: decreased 90% B to 65% from 0 to 7 min, further decreased B to 50% from 7 to 7.5 min, then held 50% B for 2.5 min with the post time for 7 min. The injection volume was 2 μL.

Data acquisition was performed using a 6546 series quadrupole time-of-flight mass spectrometer (Agilent, Santa Clara, CA) in positive and negative ion modes. The detailed parameters for mass spectrometry analysis were given as follows: Gas temperature 300°C, drying gas flow 8 L/min, sheath gas temperature 325°C, Sheash gas flow 11 L/min, Vcap 3500V, spray voltage 500 V for positive and 1000 V for negative.

Data processing was conducted with Profinder 10.0 software (Agilent, Santa Clara, USA). Information for peak extraction including retention time and exact mass was used according to the compound list included in the method. The software parameters used for metabolite extraction were as follows: Mass tolerance (ppm): 30, Retention time tolerance (min): 0.1, Absolute height > = 200 counts, Maximum

number of peaks: 5, Chromatogram data format: Centroid, Spectra to include: At apex of peak, TOF spectra: In the m/z ranges used in the chromatogram, Maximum spike width: 2, Required valley: 0.7.

CE – TOF/MS Analysis

The experiment utilized a capillary electrophoresis system (CE, #G7100A, Agilent) paired with a 1260 ISO pump (Agilent, #G1310B) and a time-of-flight mass spectrometry system (TOF/MS, Agilent, #G6224A), along with an electrophoresis-electrospray ionization-MS spray kit (Agilent, #G1607A). The connection between the capillary electrophoresis and the mass spectrometer was established using Agilent's coaxial sheath fluid interface. Control of both CE and MS was conducted through ChemStation software (Agilent, B.04.03) and Mass Hunter Workstation software (Agilent, B.04.00). Metabolomics data were collected in both cation-positive (CP) and anion-negative (AN) modes. The original CE-TOF/MS analysis data underwent processing with Qualitative Analysis (Agilent, B.04.00), Quantitative Analysis (Agilent, B.04.00), and MethodMarker software (Human Metabolome Technologies). Metabolite identification was based on a database consisting of 500 standards. Prior to statistical analysis, the exported data were sequentially normalized using internal standards.

Reducing/Non-reducing Immunoblot

The processed non-reduction or reduction protein samples were run on protein electrophoresis (4%-20% PrecastGel, Tanon). The protein in the gel was then transferred to an NC (nitrocellulose) membrane (Millipore, Danvers, MA). Then, the NC membrane was incubated in 5% non-fat milk in PBST (PBS + 0.5% Tween20) for 1 h at room temperature. Subsequently, the membrane was washed twice with PBST for 5 min each. Next, the membrane was incubated with the appropriate antibody overnight at 4°C. Primary antibody from ABclonal included MYH9 (#: A0173), FLNA (#:A3738), Drebrin (#:A6336), Flag(#:AE063), MDH1(#:A9673), IDH1 (#:A13245), IDH2 (#:A11270), SDHB (#:A1809), FH (#:A21403), GADPH (#:AC001), Bax (#:A0207); HUABIO: BAK (#:721051), MYO19 (#:ER65629), TLN1 (#:ET1608-21), Caspase-1 (#: ET1608-69), Caspase-2 (#:ET1602-30), Caspase-3 (#:ET1602-39), Caspase-6 (#:ET1610-24), Caspase-7 (#:ET1612-28), Capspase-8 (#:ET1603-16), Caspase-9 (#:ET1610-95), Caspase-10 (#: ET1701-53). Primary antibodies from Cell Signaling Technology included SLC7A11 (#:98051), SLC3A2 (#:13180), AMPKα (#: 2532), Phos-AMPK (Thr 172) (#:2535), PARP (#:9532), Cleaved-Caspase3 (#:9664); Vinculin (Santa cruz, #: sc-73614). The next day, the membrane was washed with PBST 3 times (5 min each). The membrane was then incubated with the secondary antibody (1:5,000 dilution in PBST) for 1 h at room temperature. Secondary antibody from Goat anti-Rabbit IgG (H + L) Poly-HRP Secondary Antibody (Invitrogen, #: 32260), Goat anti-Mouse IgG (H + L) Poly-HRP Secondary Antibody (Invitrogen, #: 32230). After incubation, the membrane was washed with PBST 3 times (5 min each time), and the membrane was visualized using a fully automated chemiluminescence image analysis system (Tanon-5200).

Immunofluorescence

Cells were seeded on a microscope glass slide in the 12-well chamber plate and cultured overnight. The next day, the plate was washed twice with PBS after removing the medium. Cells were fixed with 4%

paraformaldehyde for 15 min. For staining of F-actin, the cytoskeleton was labeled with 1×CellMask™ Actin Tracking Stains (Invitrogen, #: A57246) for 1 h. After staining, the cells were washed with PBST 3 times (20 s each time), and then stained with DAPI. For protein localization assay, the cells were blocked with 5% BSA in PBS for 20 min. After blocking, cells were incubated in primary antibody (SLC3A2 or Tomm20) and secondary antibody for 1 h at room temperature with sequential washing with PBST 3 times (2 min each time) in between incubation steps. After final washing, slides were mounted with glycerol and observed with two-photon laser Confocal microscopy.

Live Cell Imaging

UOK262 cells were seeded in a 60 mm culture dish and allowed to adhere overnight. Following F-actin staining, the cells were cultured in a glucose-free medium containing 10 μg/mL of Propidium iodide (PI) for observation. Images of the cells were captured in a 5% CO_2, 37°C incubator with a ZEISS Cell Observer SD (Germany) using a time-lapse setting of 10 minutes per frame over 24 h.

Cell death assay

After the cells had been treated with the indicated conditions. Fumarate hydratase-IN-1 (MCE, #: HY-100004), JX06 (MCE, #: HY-100004), Necrostatin-1 (MCE, #: HY-15760), Necrostatin-2 (MCE, #: HY-14622), Ferrostatin-1 (MCE, #: HY-100579), Z-VAD-FMK (MCE, #: HY-16658B), Chloroquine (MCE, #: HY-17589A), 2-Deoxy-D-glucose (MCE, #: HY-13966), Rotenone (MCE, #: HY-B1756), Tempol (MCE, #: HY-100561), Trolox (MCE, #: HY-101445), Staurosporine (MCE, #: HY-15141), Antimycin A (GLPBIO, #: GC49360), Atpenin A5 (MCE, #: HY-126653), TCEP hydrochloride (MCE, #: HY-W011500), DL-dithiothreitol (DTT) (MCE, #: HY-15917). PI was added to the culture medium at a working concentration of 50 μg/mL for 20 min. Cells and medium was collected, followed by flow cytometry to detect the percentage of PI-positive cells.

For clone formation assay, UOK262 cells were seeded into the appropriate wells of a plate. After treatment under the specified conditions, the culture medium was removed, and the wells were washed twice with PBS. Then, 4% paraformaldehyde was added for fixation for 10 min. Following fixation, the wells were washed twice with PBS. Next, the cells were incubated with crystal violet solution for 10 min. After incubation, the wells were washed with PBS, air-dried, and photographed.

For compound library screening assay, UOK262 cells were seeded at 10,000 cells per well in a 96-well plate, with three technical replicates for each experiment. A 10 μM working concentration of compounds from the compound library was prepared in glucose-free medium. The control group was treated with glucose-free medium containing DMSO. After 12 h of incubation, CCK-8 reagent was added at a 1:10 ratio (CCK-8: medium) and incubated for 2 h. The absorbance was then measured at 450 nm to assess cell viability.

Mitochondrial isolation

Mitochondria were isolated using a commercial isolation kit. Briefly, cells were washed with PBS, digested with trypsin-EDTA solution (100–200 g) and centrifuged at room temperature for 5–10 min.

Then 1-2.5 mL of Mitochondrial Isolation Reagent (both supplemented with PMSF) was added to 20–50 million cells. Cells were gently resuspended and placed on ice for 10–15 min. The cell suspension was homogenized about 10–30 times and centrifuged at 600 g for 10 min at 4°C. Supernatant was carefully transferred to another tube, and centrifuged at 11,000 g for 10 min at 4°C. The remaining pellet contained the isolated cellular mitochondria, whereas the collected supernatant was centrifuged at 12000 g for 10 min at 4°C for isolation of cytosolic proteins.

Quantitative proteomics

For sample preparation, UOK262 cells or mitochondria from MCF-7 cells, were suspended in lysis buffer (1% sodium deoxycholate (SDS), 8 M urea) with 1x protease inhibitor cocktail. Samples were sonicated for 2 min, then lysed samples were placed at 4°C for 30 min. After centrifugation at 16,000 g for 20 min at 4°C, protein supernatant concentrations were measured by the bicinchoninic acid (BCA) method using a commercial protein assay kit. Sample preparation methods include protein denaturation, reduction, alkylation, as well as trypsinization and peptide purification. A commercial iST sample preparation kit (PreOmics, Germany) was used according to the manufacturer's protocol. Briefly, 50 µL of lysis buffer was added and then heated to 95°C for 10 min while stirring at 1,000 rpm. After the samples cooled to room temperature, trypsin digestion buffer was added and incubated for 2 hours at 37°C, 500 rpm, with agitation.

For peptide digestion, peptides were redissolved in solvent A (A: 0.1% formic acid in water) and analyzed by Tandem EASY-nanoLC1200 with Orbitrap Fusion Lumos (Thermo Fisher Scientific, MA, USA). 2 µL of peptide sample was loaded onto a 25 cm analytical column (75 µm inner diameter, 1.9 µm resin) and suspended in 4% buffer B (80% ACN, 0.1% FA) with a gradient of 130 min. The gradient was gradually increased to 50% B at interval of 5 min, gradually increased to 95% B at intervals of 1 min, and kept for 9 min. The column flow rate was set to 250 nL/min and the column temperature was maintained at 55°C. The electrospray voltage was set at 2 kV. For nano-HPLC-MS/MS analysis, a hybrid data strategy was used, operated in a data collection and agnostic mode. Search scans were recorded at 120K resolution with a 1e6 AGC target and a maximum injection time of 100 ms. A variable separation window was applied to the DIA MS2 acquisition. The full scan was followed by 20 windows with a resolution of 50,000, a target AGC of $1e^5$, a maximum injection time of 86 ms, and a normalized collision energy of 33%.

For data analysis, raw DIA data were processed and analyzed using Spectronaut 17 (Biognosys AG, Switzerland) with default settings. The analysis aimed to search the Homo sapiens protein database (version 2022, entry 20610). Cysteine carbamoyl-urea was identified as an immobilization modification. Oxidation to methionine was assigned as a variable modification. Data extraction was determined by Spectronaut based on various mass calibrations. The optimal extraction window was dynamically determined using Spectronaut-based iRT calibration and gradient stability. The Q-value cutoff (FDR) was 1% at the parental level and 1% at the protein level. Decoy generation was set to Mutation. This was similar to shuffling, but only applying a random number of AA positions to swamp (min = 2, max =

length/2). The normalization strategy was defined as local normalization. For peptides with Q values above the critical 1% the number of major groups was calculated using the MaxLFQ method.

The protein-protein interaction network construction

For the interaction protein network analysis of the oxidative proteomics, 58 commonly upregulated proteins between UOK262 cells and SLC7A11-overexpressing 786-O cells were analyzed using the STRING database. For the interaction protein network analysis of the mitochondria, rhe protein-protein interaction network was obtained from the STRING database (https://cn.string-db.org/cgi/download?sessionId=b3I5jvJ3jUu5) as the biological background network. The information regarding the mitochondrial proteome was collected from the MitoCarta 3.0 database (http://www.broadinstitute.org/mitocarta). By combining the selected core proteins with the mitochondrial proteome, a subnetwork of proteins was extracted from the background network (with a combined score > = 0.4). After calculating the fold change (FC) and p-value, all proteins were categorized into three groups: Up-regulated (FC > 1.1 and $p < 0.05$), down-regulated (FC < 0.9 and $p < 0.05$), and no significant change ($p > 0.05$ or 0.9 < FC < 1.1). The final network was visualized using RStudio and the 'graph' package.

NADP(H) and NAD(H) measurements

NADP(H) was detected with the NADP(H) assay kit (Elabscience Cat#: E-BC-K803-M). Briefly, after removing culture medium, cells on the 6-well plate were washed with pre-chilled PBS on ice. The cells were scraped with a cell scraper, then 2 mL of pre-cooled PBS on ice and the cells were collected by centrifugation at 1,000 g at 4°C for 10 min. Reagent I (0.2 mL) was added to lyse the cells for 10 min. For NADPH measurement, the cell lysate was heated in a water bath at 60°C for 30 min and then centrifuged at 10,000 g for 10 min, and the supernatant was taken for further determination. For total NADP(H) measurement, 50 μL of cell lysate and 100 μL of reaction working solution were added to the enzyme plate. After shaking the plate for 5 s, it was incubated in a 37°C oven for 10 min. Then 20 μL of Reagent III was added, the plate was shaken for 5 seconds, and the sample was further incubated at 37°C for 10 min and measured at 450 nm. NAD(H) levels were calculated according to the formula provided by the kit (Elabscience Cat#: E-BC-K318-M).

ROS analysis

To measure cellular ROS levels, we employed the DCFH-DA (2',7'-dichlorodihydrofluorescein diacetate) probe (MCE, #: HY-D0940) and flow cytometry. Cells (Vector, KD-FH, Overexpression Oe SLC7A11 786-O) were seeded in culture dishes and grown to approximately 70–80% confluence. Following glucose starvation for 5 h, cells were washed with PBS to remove residual culture medium. The cells were then stained with a 10 μM solution of DCFH-DA and incubated at 37℃ with 5% CO_2 for 30–60 min. After staining, the cells were washed again with PBS to remove any unbound probes.

Cells were collected and resuspended in PBS at a concentration of 1×10^6 cells/mL. Flow cytometry analysis was performed with the parameters set to measure forward scatter (FSC), side scatter (SSC),

and fluorescence in the FITC channel, which detects DCF fluorescence. The results were presented as peak plots, with fluorescence intensity values on the x-axis. For each group, 5,000 cells were utilized, and the experiment was repeated three times, and the statistical significance of fluorescence intensity was assessed.

Molecular Docking

The amino acid sequence of Caspase-3 from the UniProt database (https://www.uniprot.org/) was retrieved, ensuring that the sequence is complete, without any missing regions or mutations. Then, the sequence was uploaded to AlphaFold2 (https://alphafold.com/) to predict the 3D structure of the protein. Next, we utilized the Swiss-Model platform (https://swissmodel.expasy.org/) for homology modeling by selecting an appropriate template (a homologous Caspase-3 protein) to generate another 3D structure. Using the predicted monomer structures, we proceeded to build the Caspase-3 dimer in molecular docking software. Energy minimization was performed using molecular dynamics simulation software to ensure the stability of the dimer structure. The results revealed that during the formation of the human-derived Caspase-3 dimer, two sets of disulfide bonds are formed between chain A and chain B, promoting the formation of a stable dimer structure. Specifically, the two sets of disulfide bonds involve Cys184 on chain A and Cys264 on chain B.

Mitochondria membrane potential analysis.

Cultured HeLa cells in 6-well plate until they reach 70–80% confluence. Then, Mitotracker and Tetramethylrhodamine ethyl ester (TMRE) solution were added to the cells and incubated for 30 min at 37°C in a CO_2 incubator. After incubation, cells were gently washed with PBS to remove excess dye. Cells were resuspended in PBS for flow cytometry analysis at 488nm for Mitotracker and 543 nm for TMRE fluorescence detection.

Declarations

Funding Statement

The study has been supported by the foundation (No. 21934006) from the National Natural

Science Foundation of China, Strategic Priority Research Program (B) of Chinese Academy of

Sciences (XDB38020200), the Youth Innovation Promotion Association CAS

(2021186) and the innovation program (DICP I202334) of science and research from the DICP,

CAS.

Author Contributions

Conceptualization, G.W.X.; Data curation, P.D., X.L., P.Y.G., M.B., X.G., and X.Y.L.; Formal analysis, P.D., P.Y.G., X.L., S.M.P., L.N.Z., H.L., and Z.K.L., F.T.C.; Methodology, P.D., M.B., X.G., T.W., J.H.Z., Q.L., J.W.H., and D.J.; Writing—original draft, P.D., Y.C., X.L., and M.B.; Writing—review & editing, X.Q., Z.P.Z., Y.C. and G.W.X. All authors have read and agreed to the published version of the manuscript.

Institutional Review Board Statement

Not applicable.

Informed Consent Statement

Not applicable.

Data Availability Statement

All relevant data are within the paper.

Conflicts of Interest

The authors declare no conflict of interest.

References

1. Faubert B, Solmonson A, DeBerardinis RJ (2020) Metabolic reprogramming and cancer progression. Science 368
2. Li H et al (2019) The landscape of cancer cell line metabolism. Nat Med 25:850–860
3. Pan C, Li B, Simon MC (2021) Moonlighting functions of metabolic enzymes and metabolites in cancer. Mol Cell 81:3760–3774
4. Koppula P, Zhang Y, Zhuang L, Gan B (2018) Amino acid transporter SLC7A11/xCT at the crossroads of regulating redox homeostasis and nutrient dependency of cancer. Cancer Commun (Lond) 38:12
5. Lang X et al (2019) Radiotherapy and Immunotherapy Promote Tumoral Lipid Oxidation and Ferroptosis via Synergistic Repression of SLC7A11. Cancer Discov 9:1673–1685
6. He F et al (2023) ATF4 suppresses hepatocarcinogenesis by inducing SLC7A11 (xCT) to block stress-related ferroptosis. J Hepatol 79:362–377
7. Liu X et al (2023) Actin cytoskeleton vulnerability to disulfide stress mediates disulfidptosis. Nat Cell Biol 25:404–414
8. Sciacovelli M et al (2016) Fumarate is an epigenetic modifier that elicits epithelial-to-mesenchymal transition. Nature 537:544–547
9. Ge X et al (2022) Fumarate inhibits PTEN to promote tumorigenesis and therapeutic resistance of type2 papillary renal cell carcinoma. Mol Cell 82:1249–1260e1247

10. Sulkowski PL et al (2020) Oncometabolites suppress DNA repair by disrupting local chromatin signalling. Nature 582:586–591
11. Pollard PJ et al (2005) Accumulation of Krebs cycle intermediates and over-expression of HIF1alpha in tumours which result from germline FH and SDH mutations. Hum Mol Genet 14:2231–2239
12. Laukka T et al (2016) Fumarate and Succinate Regulate Expression of Hypoxia-inducible Genes via TET Enzymes. J Biol Chem 291:4256–4265
13. Cheng J et al (2023) Cancer-cell-derived fumarate suppresses the anti-tumor capacity of CD8(+) T cells in the tumor microenvironment. Cell Metab 35:961–978e910
14. Shimizu Y, Hendershot LM (2009) Oxidative folding: cellular strategies for dealing with the resultant equimolar production of reactive oxygen species. Antioxid Redox Signal 11:2317–2331
15. Olson MF (2008) Applications for ROCK kinase inhibition. Curr Opin Cell Biol 20:242–248
16. Sebbagh M et al (2001) Caspase-3-mediated cleavage of ROCK I induces MLC phosphorylation and apoptotic membrane blebbing. Nat Cell Biol 3:346–352
17. Bock FJ, Tait SWG (2020) Mitochondria as multifaceted regulators of cell death. Nat Rev Mol Cell Biol 21:85–100
18. Wu YQ et al (2023) Low glucose metabolite 3-phosphoglycerate switches PHGDH from serine synthesis to p53 activation to control cell fate. Cell Res 33:835–850
19. Weindel CG et al (2022) Mitochondrial ROS promotes susceptibility to infection via gasdermin D-mediated necroptosis. Cell 185:3214–3231e3223
20. Evavold CL et al (2021) Control of gasdermin D oligomerization and pyroptosis by the Ragulator-Rag-mTORC1 pathway. Cell 184:4495–4511e4419
21. Patra KC, Hay N (2014) The pentose phosphate pathway and cancer. Trends Biochem Sci 39:347–354
22. Zheng L et al (2015) Fumarate induces redox-dependent senescence by modifying glutathione metabolism. Nat Commun 6:6001
23. Zheng L et al (2023) Circulating succinate-modifying metabolites accurately classify and reflect the status of fumarate hydratase-deficient renal cell carcinoma. J Clin Invest 133
24. Mullen AR et al (2011) Reductive carboxylation supports growth in tumour cells with defective mitochondria. Nature 481:385–388
25. Fu X et al (2015) 2-Hydroxyglutarate Inhibits ATP Synthase and mTOR Signaling. Cell Metab 22:508–515
26. Salamanca-Cardona L et al (2017) In Vivo Imaging of Glutamine Metabolism to the Oncometabolite 2-Hydroxyglutarate in IDH1/2 Mutant Tumors. Cell Metab 26:830–841e833
27. Foretz M, Guigas B, Viollet B (2023) Metformin: update on mechanisms of action and repurposing potential. Nat Rev Endocrinol 19:460–476
28. Elgendy M et al (2019) Combination of Hypoglycemia and Metformin Impairs Tumor Metabolic Plasticity and Growth by Modulating the PP2A-GSK3beta-MCL-1 Axis. Cancer Cell 35:798–815e795

29. Ying M et al (2021) Lactate and glutamine support NADPH generation in cancer cells under glucose deprived conditions. Redox Biol 46:102065
30. Shi P et al (2022) Mechanical instability generated by Myosin 19 contributes to mitochondria cristae architecture and OXPHOS. Nat Commun 13:2673
31. Kulkarni RA et al (2019) A chemoproteomic portrait of the oncometabolite fumarate. Nat Chem Biol 15:391–400
32. Liu X, Zhuang L, Gan B (2024) Disulfidptosis: disulfide stress-induced cell death. Trends Cell Biol 34:327–337
33. Xu Y et al (2023) Genomic Profiling and Response to Immune Checkpoint Inhibition plus Tyrosine Kinase Inhibition in FH-Deficient Renal Cell Carcinoma. Eur Urol 83:163–172
34. Bezwada D et al (2024) Mitochondrial complex I promotes kidney cancer metastasis. Nature 633:923–931
35. Molina JR et al (2018) An inhibitor of oxidative phosphorylation exploits cancer vulnerability. Nat Med 24:1036–1046
36. Yap TA et al (2023) Complex I inhibitor of oxidative phosphorylation in advanced solid tumors and acute myeloid leukemia: phase I trials. Nat Med 29:115–126

Figures

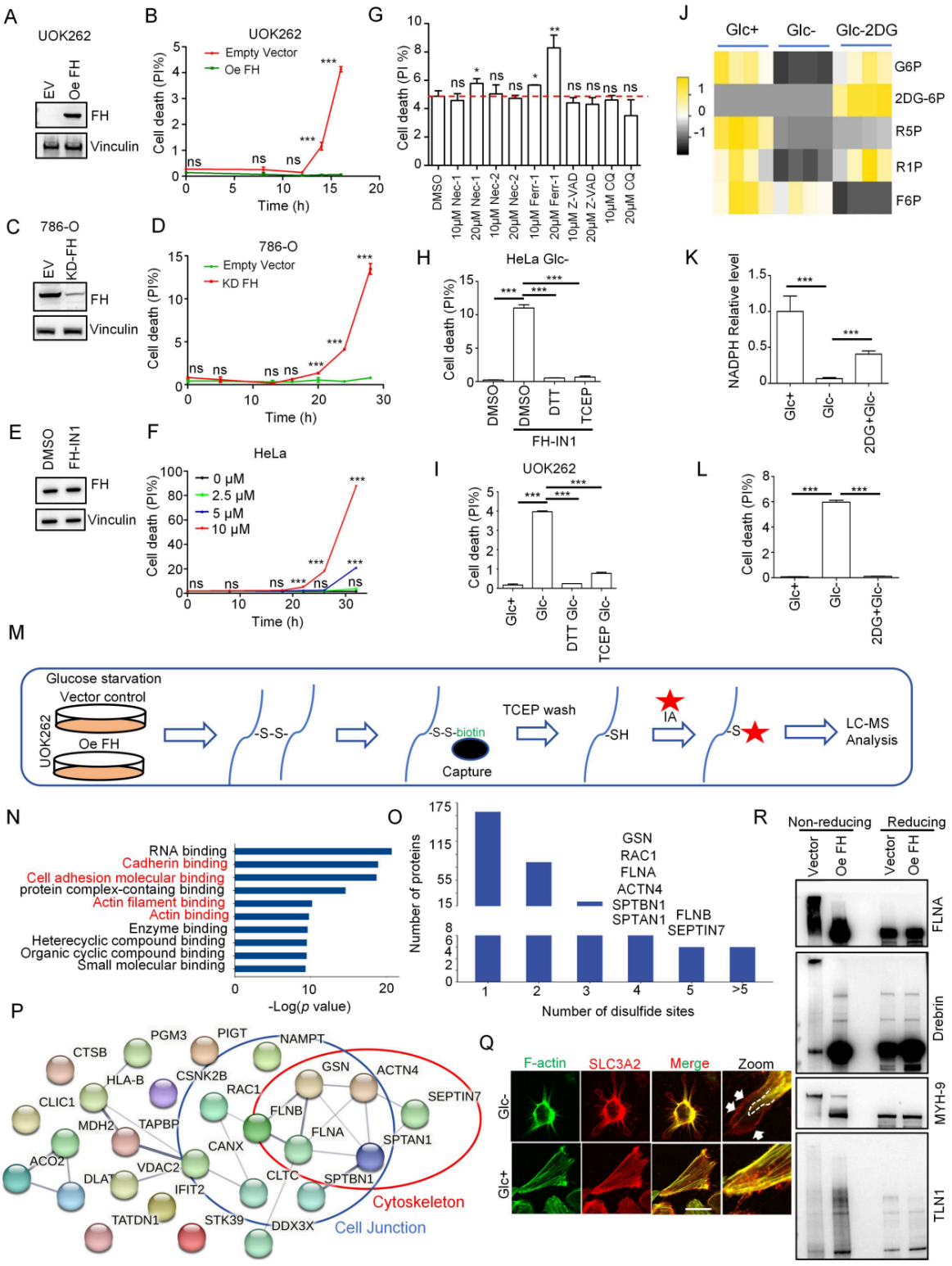


Figure 1

FH deficiency drives cellular actin cytoskeletal polymerization under glucose starvation.

(A) Immunoblot analysis of FH protein levels in FH^{deficient} UOK262 cells with vector control or FH over-expression (Oe FH). Vinculin serves as a loading control.

(B) Evaluation of cell death (PI-positive staining) in vector control and FH over-expressing UOK262 cells cultured in glucose-free medium for the indicated durations.

(C) Immunoblot analysis of FH protein levels in 786-O cells with vector control and knockdown of FH (FH-KD).

(D) Assessment of cell death (PI-positive staining) in vector control, FH-KD 786-O cells under glucose-free conditions over the specified time points.

(E) Immunoblot analysis of FH protein levels in HeLa cells with DMSO or FH-IN1 (10 μM) treatment.

(F) Cell death (PI positive) in HeLa cells cultured in glucose-free medium and containing 0, 2.5, 5, 10 μM FH-IN1 for the indicated times.

(G) Cell death in HeLa cells cultured in glucose-free medium with indicated programmed cell death inhibitors: Ner-1 and Ner-2, necrosis inhibitors; Ferr-1, ferroptosis inhibitor; Z-VAD, apoptosis inhibitor; or CQ, autophagy inhibitor for 22 hours. The red dashed line represents the proportion of cell death induced by glucose-free medium with 10 μM FH-IN1.

(H) Cell death in HeLa cells cultured in glucose-free medium with or without 10 μM FH-IN1, 2 mM DTT or 1 mM TCEP for 22 hours.

(I) Cell death in $FH^{deficient}$ UOK262 cells cultured in glucose-free medium with or without 2 mM DTT or 1 mM TCEP for 16 hours.

(J-K) Relative metabolite levels of glucose metabolism in $FH^{deficient}$ UOK262 cells when treated in the following conditions: glucose-containing, glucose-free, glucose-free with 2mM 2DG for 12 hours. Heap map depicts the metabolites of the glycolysis and the PPP pathways (J). Relative NADPH levels in each of these three conditions are provided, relative to glucose treated cells (K).

(L) Cell death in $FH^{deficient}$ UOK262 cells cultured in glucose-containing and glucose-free medium with or without 2 mM 2DG treatment for 18 hours.

(M) Flowchart illustrating redox proteomics analysis performed on vector control and FH over-expressing UOK262 cells. (Iodoacetamide, IA; Liquid Chromatography-Mass Spectrometry, LC-MS)

(N) Gene Ontology analysis of the proteins associated with the cysteine-containing peptide in (Vector control vs Oe FH, FC>1.5) UOK262 cells.

(O) The number of disulfide sites in up-regulated proteins in $FH^{deficient}$ UOK262 cells.

(P) Protein-protein interaction (PPI) network analysis of up-regulated cysteine-containing proteins (disulfides number ≥ 4) in the context of vector control UOK262 cells. Cell junction (blue circle) and cytoskeletal protein (red circle) networks are represented.

(Q) Images of F-actin and SLC3A2 in UOK262 cells cultured in glucose-containing and glucose-free medium for 12 hours. The white box indicates the region of interest depicted in the images to the right. White arrow highlights the cell membrane, and the white dashed line depicts the contracted F-actin. Scale bar (20 μm).

(R) Reducing/non-reducing immunoblots showing actin cytoskeleton proteins (FlNA, Drebrin, TLN1, and MYH9) in vector control (Vector) and FH overexpressing (Oe FH) UOK262 cells cultured in glucose-free medium for 12 hours.

P-values were obtained by the two-tailed Students' t-test. Data are presented as mean ± SD; n=3

independent repeats, ns: not significant, ***p<0.001.

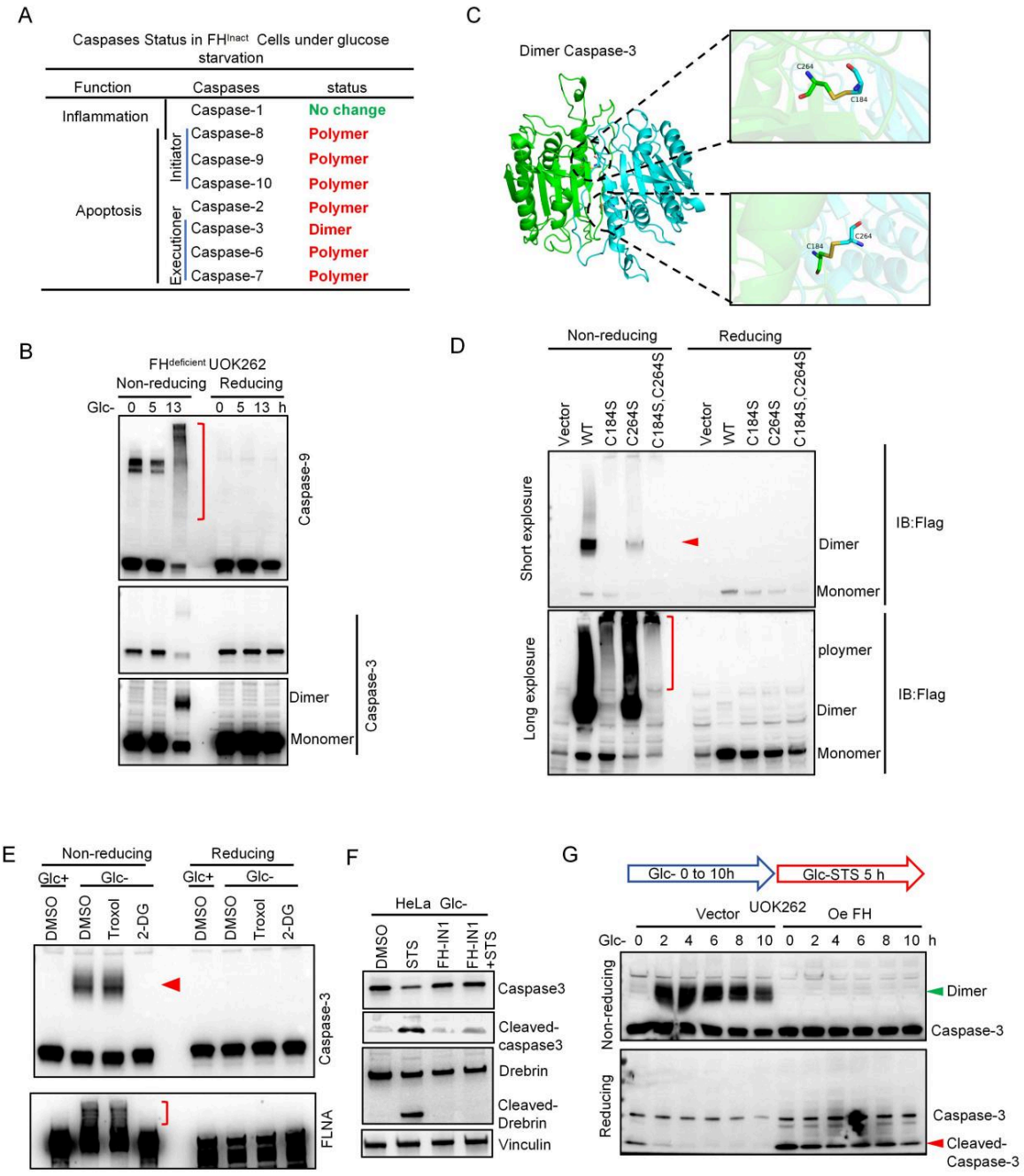


Figure 2

Disulfide stress results in the inactivation of various caspases.

(A) States of caspases during glucose starvation-induced disulfide stress in FH^{Inact} HeLa cells. (Red indicates altered caspase levels, while green denotes unchanged caspase levels).

(B) Reducing/non-reducing immunoblots showing the activation states of Caspase-9 and Caspase-3 in $FH^{deficient}$ UOK262 cells cultured in glucose-free medium for the indicated times.

(C) Molecular docking analysis showing Caspase-3 dimer formation through cysteine residues at positions 264 and 184.

(D) HEK293T cells expressing vector, Flag-tagged Caspase-3, or Flag-tagged Caspase-3 with cysteine-to-serine mutations (C264S and C184S) were cultured in glucose-free medium with 10 μM FH-IN1 for 16 hours. Reducing/non-reducing immunoblots showing Caspase-3 dimerization (Triangle highlights the dimer Caspase-3 and the brackets denotes Caspase-3 polymers).

(E) Reducing/non-reducing immunoblots showing $FH^{deficient}$ UOK262 cells cultured in glucose-containing or glucose-free medium for 12 hours with the indicated treatments. Treatments include 10 μM FH-IN1, 25 μM Troxol and 2 mM 2DG. Triangles mark the Caspase-3 dimer and the brackets illustrate FLNA polymers).

(F) Activation of apoptosis signaling in HeLa cells under the indicated conditions. DMSO: glucose-free medium for 16 hours. FH-IN1: glucose-free medium with 10 μM FH-IN1 for 16 hours. FH-IN1+STS or STS only: glucose-free medium with 10 hours of FH-IN1 treatment followed by 1 μM STS treatment for 6 hours.

(G) Reducing/non-reducing immunoblots illustrating the activation of Caspase-3 in vector control UOK262 and FH over-expressing UOK262 cells under the indicated conditions. Cells were cultured in glucose-free medium for various times (0 to 10 hours) and treated with STS for 5 hours.

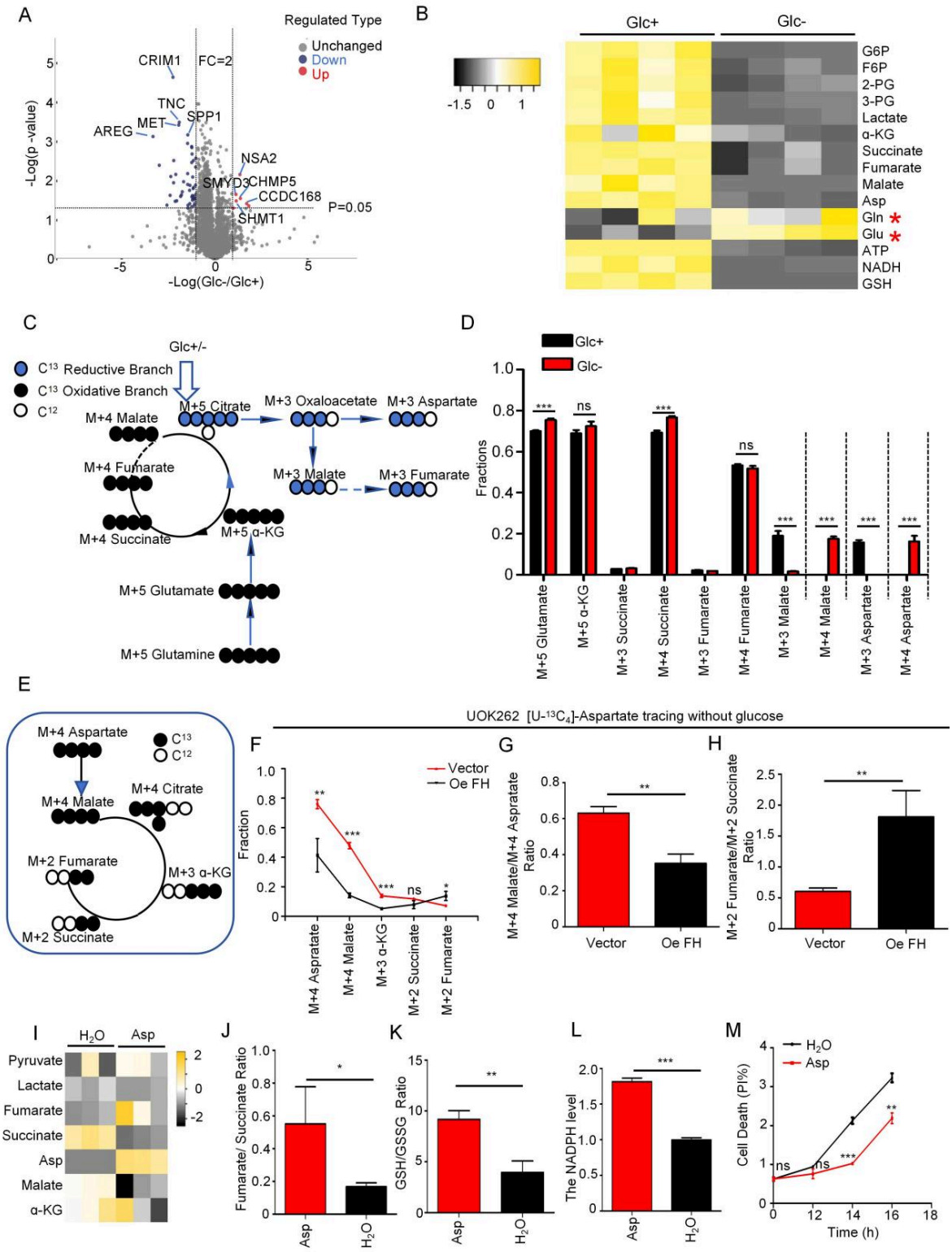


Figure 3

FH deficiency inhibits the reductive and enhances oxidative TCA cycle under glucose starvation

(A) Volcano plot of the proteome in FH^{deficient} UOK262 cells cultured in glucose-containing or glucose-free medium. Green and red points represent significantly altered protein expression (P≤0.05, fold change (FC) > 2).

(B) Heatmap showing alterations in the indicated metabolites in $FH^{deficient}$ UOK262 cells cultured in glucose-containing or glucose-free medium for 12 hours. The red star highlights glutamine and glutamate overproduction in glucose free conditions.

(C) Diagram illustrating the number of carbon isotopes in metabolites of the reductive and oxidative TCA cycles labeled with U-$^{13}C_5$-glutamine (Blue solid circles indicate ^{13}C-containing metabolites in the reductive TCA cycle).

(D) Metabolic flux changes in $FH^{deficient}$ UOK262 cells cultured in glucose-containing or glucose-free medium with [U-$^{13}C_5$]-glutamine labeling for 8 hours.

(E) Schematic diagram of the metabolic flow of [U-$^{13}C_4$]-aspartate (Asp). Black and white solid circles represent ^{13}C and ^{12}C-containing metabolites, respectively.

(F-H) Metabolic flux changes in vector control and FH over-expressing UOK262 cells cultured in glucose-free media with 20 mM [U-$^{13}C_4$]-aspartate for 8 hours. (F) Effect of FH deficiency on the oxidative TCA cycle branch (from aspartate to fumarate). (G) Ratio of M+4 aspartate to M+4 malate. (H) Ratio of M+4 fumarate to M+4 succinate.

(I-L) Relative levels of TCA cycle metabolites in $FH^{deficient}$ UOK262 cells cultured in glucose-free medium with or without 20 mM aspartate (Asp) treatment for 10 hours. (I) Heatmap illustrating changes in indicated metabolites. (J) Ratio of fumarate to succinate. (K) Ratio of GSH to GSSG.

(L) The NADPH level in UOK262 cells cultured in glucose-free medium with or without 20 mM aspartate (Asp) treatment for 12 hours.

(M) Cell death in UOK262 cells cultured in glucose-free medium with or without 20 mM aspartate treatment for the indicated times.

P-values were obtained by the two-tailed Students' t-test. Data are presented as mean ± SD; n=3. independent repeats, for (D) n=4, ns: not significant, *p<0.05, **p<0.01, ***p<0.001.

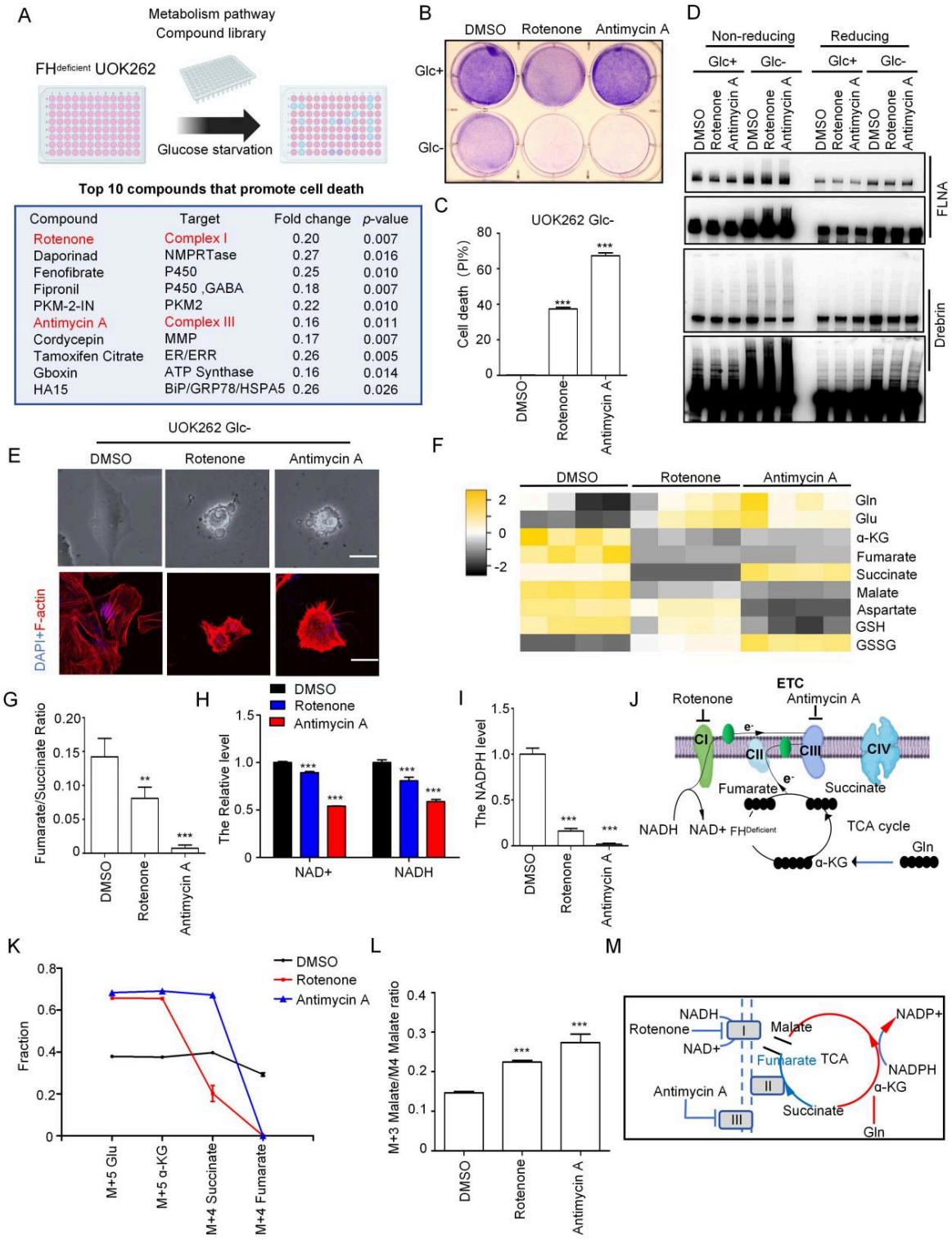


Figure 4

Targeting mitochondrial complexes cause disulfide stress acceleration in FH^{deficient} cells under glucose starvation.

(A) Screening of a 200-compound library to identify targets that promote cell death in FH^{deficient} cells under glucose starvation conditions. FH^{deficient} UOK262 cells were treated with compounds at a

concentration of 10 μM under glucose starvation for 12 hours, and cell viability was measured using the CCK-8 assay; n=3, p-values were obtained by the two-tailed Students' t-test.

(B) $FH^{deficient}$ UOK262 cells were cultured in glucose-containing or glucose-free culture medium with 1 μM Rotenone or Antimycin A treatment for 12 hours and clone formation analyzed cell survival.

(C) Cell death in $FH^{deficient}$ UOK262 cultured in glucose-free medium for 12 h with 1 μM Rotenone, 1 μM Antimycin A treatment, respectively.

(D) Reducing/non-reducing immunoblot showing the FLNA, Drebrin state in $FH^{deficient}$ UOK262 with the indicate treatment. (Glucose-containing or glucose-free medium with 1 μM Rotenone, 1 μM Antimycin A).

(E) Image of morphology and confocal image of F-actin in $FH^{deficient}$ UOK262 cells cultured in glucose-free medium with the indicated treatment for 6 h. (1 μM Rotenone, 1 μM Atpenin A5, 1 μM Antimycin A).

(F-I) $FH^{deficient}$ UOK262 cells cultured in glucose- free medium for 5 hours with the 1 μM Rotenone, and 1 μM Antimycin A treatment, respectively. (F) Heatmap showing alterations in indicated metabolites after complex I and III inhibition by the following drugs: DMSO, Rotenone, Antimycin A. (G) The ratio of fumarate to succinate. (H) NAD+ and NADH were analyzed. (I) The relative NAPDH level compared to DMSO.

(J) Schematic diagram of the action of complex I and III inhibitors.

(K-L) $FH^{deficient}$ UOK262 cells cultured in glucose-free medium containing 2 mM [U-$^{13}C_5$]-glutamine for 5 h with the 1 μM Rotenone, 1 μM Atpenin A5, 1 μM Antimycin A treatment, respectively. (K) Oxidative TCA branch (M+5 α-KG to M+4 fumarate) were analyzed. (L) The ratio of M+3 malate to M+4 malate.

(M) Metabolic pathway diagram illustrating how complex I and III inhibition promotes the reductive TCA branch in $FH^{deficient}$ UOK262 cells under glucose starvation. Red indicates enhanced reductive TCA branch, and blue indicates reduced succinate oxidation.

P-values were obtained by the two-tailed Students' t-test. Data are presented as mean ± SD; n=4 independent repeats, for (C) n=3, ns: not significant, *p<0.05, **p<0.01, ***p<0.001.

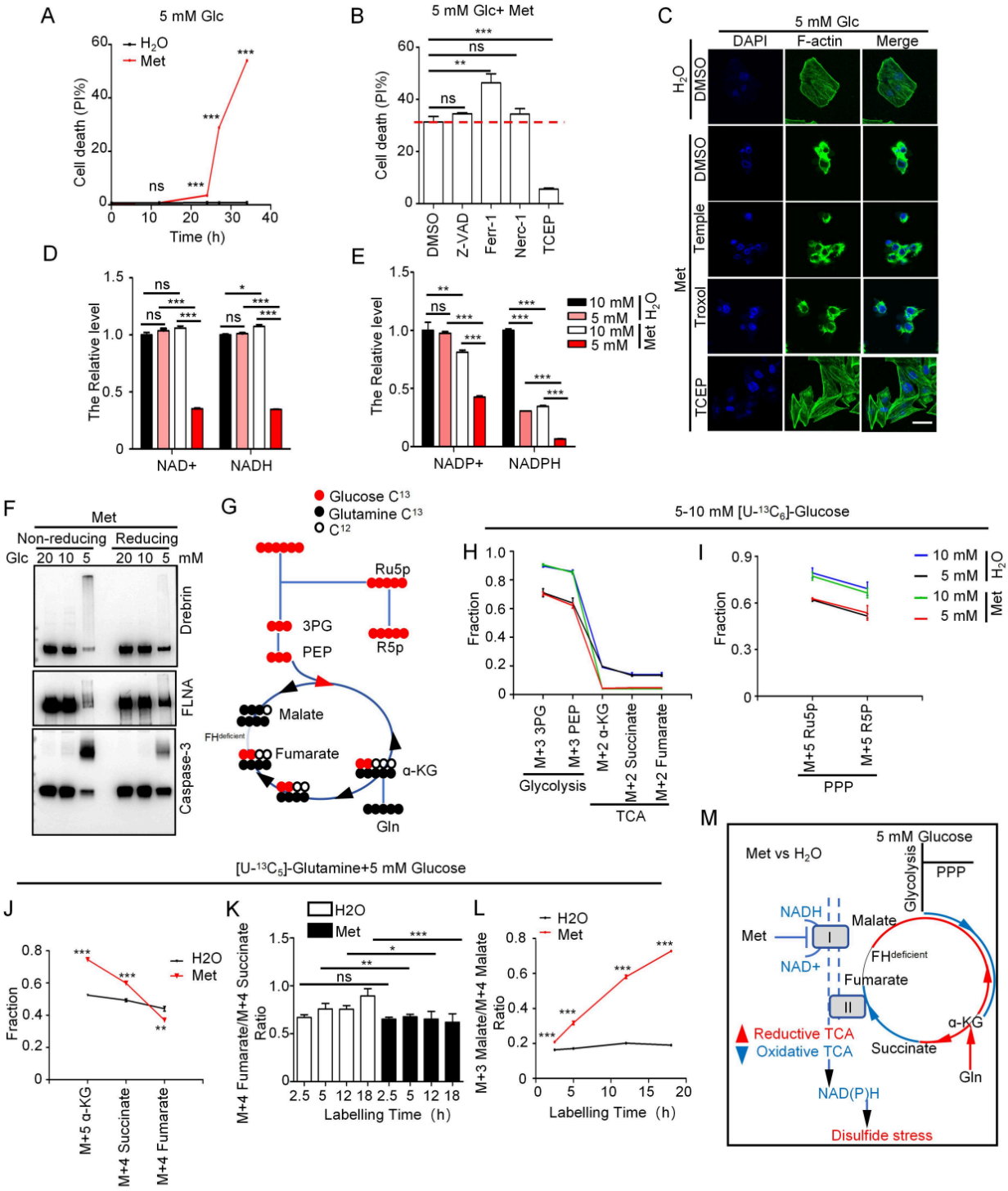


Figure 5

Metformin induces enhanced disulfide stress in FH^{deficient} cells under low glucose conditions

(A) Cell death in FH^{deficient} UOK262 cells cultured in 5 mM glucose medium with 5 mM metformin treatment for the indicated times (0, 12, 24, 27, 36 hours).

(B) Cell death in $FH^{deficient}$ UOK262 cells cultured in 5 mM glucose medium with 5 mM metformin, along with indicated programmed cell death inhibitors (10 μM Ner-1; 10 μM Ferr-1; 10 μM Z-VAD; 1 mM TCEP) for 24 hours. The red dashed line represents the proportion of cell death induced solely by 5 mM glucose and 5 mM metformin.

(C) Representative confocal images of F-actin in $FH^{deficient}$ UOK262 cells cultured in 5 mM glucose medium with the indicated conditions for 24 hours (5 mM metformin, 25 μM Troxol, 100 μM Temple, 2 mM 2DG, 1 mM TCEP). Scale bars: 10 μm.

(D-E) $FH^{deficient}$ UOK262 cells cultured in 5 mM or 10 mM glucose medium with 5 mM metformin treatment for 12 hours. (D) Measurement of the relative levels of NAD+ and NADH and (E) NADP+ and NADPH levels when compared to controls (10 mM glucose with H_2O treatment).

(F) Reducing/non-reducing immunoblots showing Drebrin, FLNA, and Caspase-3 in $FH^{deficient}$ UOK262 cells cultured in 5, 10, or 20 mM glucose with 5 mM metformin treatment for 20 hours.

(G) Metabolic flux alterations in $FH^{deficient}$ UOK262 cells cultured in glucose-free medium containing 2 mM [U-$^{13}C_5$]-glutamine or [U-$^{13}C_6$]-glucose. Black and red solid circles represent ^{13}C-containing metabolites derived from glutamine and glucose, respectively. White circles depict ^{12}C-containing metabolites.

(H-I) $FH^{deficient}$ UOK262 cells cultured in 5 mM or 10 mM [U-$^{13}C_6$]-glucose medium with or without 5 mM metformin treatment for 12 hours. (J) Relative labeling fractions of ^{13}C-metabolites from glycolysis to the oxidative TCA branch (M+3 3PG to M+2 fumarate). (K) Relative labeling fractions of ^{13}C-metabolites in the pentose phosphate pathway (PPP).

(J-L) $FH^{deficient}$ UOK262 cells cultured in 5 mM glucose and 2 mM [U-$^{13}C_5$]-glutamine medium with or without 5 mM metformin treatment. (J) Labeling fractions of ^{13}C-metabolites in the oxidative TCA branch (M+5 α-KG to M+4 fumarate). (L) Ratio of M+4 fumarate to M+4 succinate at different [U-$^{13}C_5$]-glutamine labeling times. (L) Ratio of M+3 malate to M+4 malate at different [U-$^{13}C_5$]-glutamine labeling times.

(M) Metabolic pathway diagram illustrating how metformin promotes the reductive TCA cycle and inhibits the oxidative TCA cycle in $FH^{deficient}$ UOK262 cells under low glucose conditions. Red indicates enhanced reductive TCA cycle activity, and blue indicates reduced oxidative TCA cycle activity.

P-values were obtained by the two-tailed Students' t-test. Data are presented as mean ± SD; n=3 independent repeats, For (H-I), n=5; (J-L), n=6, ns: not significant, *p<0.05, **p<0.01, ***p<0.001.

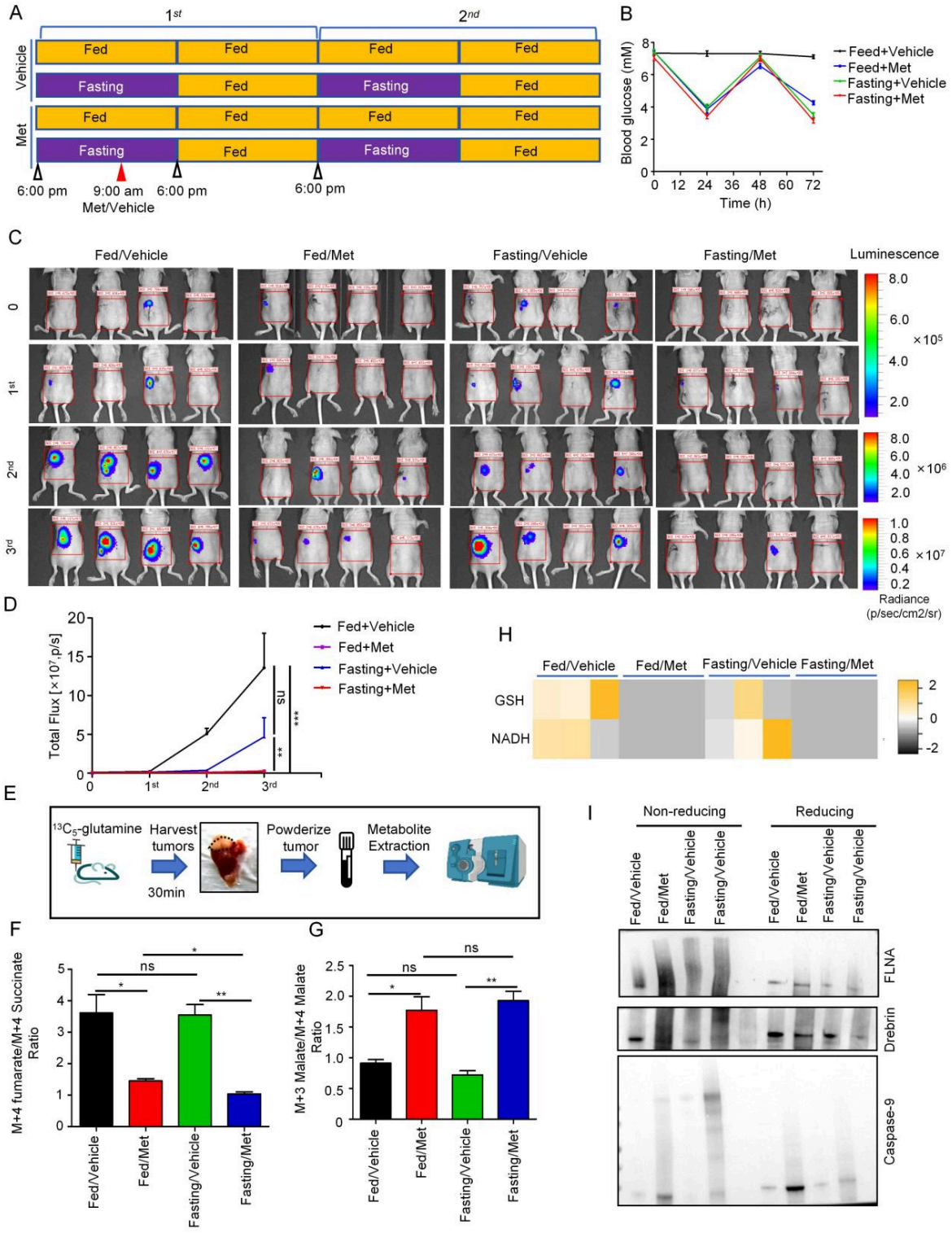


Figure 6

Metformin inhibits FH^{deficient} tumor growth

(A) Schematic diagram of tumor-bearing mouse treatment. Fasting refers to a 24-hour period of fasting (water only), followed by a 24-hour feeding period; "fed" indicates normal feeding. Blood glucose levels

of the mice are measured daily at 6:00 AM and 6:00 PM. Each treatment cycle lasts for 48 hours, and with the extension of the treatment time, it is labeled as 1^{st}, 2^{nd} and so on.

(B) Blood glucose results of mice within 72 hours after blood collection at specific time points.

(C) Representative fluorescence imaging of tumors in mice under different treatment cycles.

(D) Statistical analysis of tumor fluorescence intensity in mice under different treatment cycles.

(E) Labeling mice with [U-$^{13}C_5$]-glutamine to assess tumor metabolism. Based on the imaging results, three mice were selected for intravenous injection of 0.2 M [U-$^{13}C_5$]-glutamine, with a total of two injections. Each injection was followed by a 15-minute detection period, after which the tumors were collected for metabolic analysis.

(F) Analysis of succinate oxidation status from mice following the four feeding schemes. The ratio of M+4 fumarate to M+4 succinate is plotted.

(G) Analysis of the reductive TCA branch in the four feeding schemes. The ratio of M+3 malate to M+4 malate.

(H) Heatmap showing alterations in GSH and NADH in the indicated groups.

(I) Reducing/non-reducing immunoblot showing the FLNA, Drebrin and Caspase-9 expression in the indicated groups.

P-values were obtained by the two-tailed Students' t-test. Data are presented as mean ± SD; for (D) n=8, for (F-H) n=3, ns: not significant, *p<0.05, **p<0.01, ***p<0.001.

Supplementary Files

This is a list of supplementary files associated with this preprint. Click to download.

- TableS1.xlsx
- TableS2.xlsx
- TableS3.xlsx
- Tables4.xlsx
- Supportinginformation.docx
- Vedio1UOK262disulfidptosis.mp4